TSPE19010-055-12

남극진동이 남극기후변화 및 인도태평양에 미치는 영향 연구

Climate influence of AAO over the Antarctica and the tropical Indian-western Pacific Ocean

북경사범대학교

제 출 문

극지연구소장 귀하

본 보고서를 “남극 기후변화의 지역적 차이 원인 규명” 과제의 위탁연구 “남극진동이 남극 기후변화 및 인도태평양에 미치는 영향 연구” 과제의 최종 보고서로 제출합니다.

2020 . 2.

(본과제) 총괄연구책임자 : 김 성 중

위탁연구기관명 : 북경 사범대

위탁연구책임자 : 루이마오(Rui Mao)

1. To analyze the possible mechanisms for the linkage between the AAO and the climate over tropical Indian-Pacific Ocean

Motivation and goals:

The Antarctic Oscillation (AAO) is a pattern that involves a zonally symmetric seesaw in sea level pressure and geopotential height between polar region and middle latitudes in the Southern Hemisphere (SH). It explains the greatest proportion of the total variance of monthly SLP, zonal wind, and geopotential height in the SH. The AAO has remarkable influences on the precipitation (Reason and Rouault 2005; Silvestri and Vera 2003), surface temperature (Kwok and Comiso 2002), and storm track (Rao et al. 2003) in the Southern Hemisphere. In addition, many studies have verified that there are robust teleconnections between AAO and regional climate over the globe through the oceanic and atmospheric bridges (Dou and Wu 2018; Prabhu et al. 2016; Sun 2010; Sun et al. 2009, 2010; Zhu 2009). The AAO signals are found detectable globally in the western Pacific weather and climate components such as tropical cyclones in the Pacific and the Indian Ocean. Sun et al. (2010) have indicated that the anomalous sea surface temperature over the tropical South Atlantic Ocean associated with the boreal spring AAO can lead to anomalous Sahel rainfall in the early summer. Prabhu et al. (2016) have found that the negative phase of the AAO can induce a warming effect over the central equatorial Pacific region, and then weaken the monsoon rainfall over the Indian subcontinent. However, few studies were done concerning the relationship between AAO and tropical climate and climate extremes over the Indian-Pacific Ocean. Sea surface temperature in the Indian-Pacific Ocean is a key factor contributing to multi-seasonal to interannual climate predictability over global. Therefore, it is essential to study the teleconnection between AAO and climate over the Indian-Pacific Ocean. To address this issue, the relationship between the AAO and the atmospheric circulation, troposphere humidity, ocean heat content, and wave activity flux was investigated.

Work done and findings

1) Changes in atmospheric circulation in the Southern Hemisphere caused by AAO variations

In the positive AAO phase during August to October (ASO), an anomalous cyclonic circulation dominated in the areas from North China (NC) to the northwest Pacific, which may be a result of multiple teleconnections derived from the enhanced AAO activity (Figure 1). At least three meridional wave trains can be identified from the Indian Ocean to the Pacific. One is from the southern to equatorial Indian Ocean through South China Sea to East China Sea. The other is from the central Southern Ocean (the ocean between Australia and Antarctica) through Tasman Sea - Coral Sea to the western and northwest Pacific. The third is from Ross Sea through the central South Pacific to the east and central north Pacific. These teleconnection patterns may be motivated by an enhanced ASO-AAO and then cause an anomalous northwesterly advection from Siberia to eastern China which lead to a decrease (increase) of pollutant concentration (visibility) in NC in boreal winter.

The possible mechanism of teleconnection were also demonstrated by previous studies, although the specific subjects and the time-lag effect are different. For example, Fan and Wang (2004) suggested that the meridional teleconnection from the Antarctic to Arctic is the mechanism for the linkage between boreal winter and spring AAO and to the dust weather frequency in northern China. Furthermore, Wu et al. (2015) and Liu et al. (2015) highlighted the “memory” effect of sea surface temperature on AAO abnormal signal, namely the “ocean–atmosphere coupled bridge’’ allows the influence of the proceeding AAO to persist into for some time and affect the northern hemisphere climate. Thus the response of sea surface temperature anomaly (SSTs) to ASO-AAO were examined by analyzing the regression coefficient. For simplicity, the positive and negative regression coefficients are shaded in red and blue color, respectively (Figure 2a). The positive (negative) regression coefficients denote a sea surface warming (cooling) response to the enhanced ASO-AAO. The positive (negative) regression coefficients indicate that the ocean warming (cooling) is a response to the Antarctic oscillation. The sea surface warming from the northern Indian Ocean to Chinese coastal waters will increase the sea-land thermal contrast and sea level pressure gradient in East Asia, which in turn lead to an enhancement of East Asia winter monsoon. The enhanced East Asian winter monsoon is conducive to eliminate or mitigate air pollution in northern China (Zhang et al., 2016; Yin and Wang, 2016). On the other hand, the spatial patterns of regression coefficients are generally consistent with the three

meridional wave trains in Indian Ocean and Pacific, especially in Indian Ocean to Chinese coastal waters. For example. from Southern Ocean through southern Indian Ocean and South China Sea to East China Sea, the responses of SSTs to ASO-AAO present a “-+-+” wave pattern, which is in good agreement with the first teleconnection path mentioned above. On the other hand, the stability or continuity of the responses of the zonal mean SSTs between 45-135E to ASO-AAO were examined by lead-lag regression coefficients (Figure 2b). It can be seen that there is a good consistency of the anomalous response of SSTs to ASO-AAO from ASO (simultaneous influence) to DJF (lagged influence). Therefore, from the perspective of the temporal and spatial characteristics of the response of SSTs to ASO-AAO, the possible influence of ASO-AAO on air pollution in NC in boreal winter should be generally reliable.

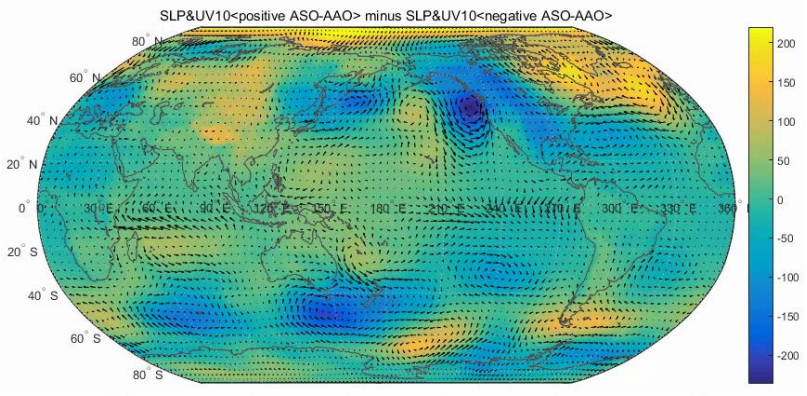

Figure 1. Composite differences of the boreal winter Sea level pressure (shading, unit is Pa) and surface winds (vectors, the maximum value is 1.45 m/s) based on ASO-AAO index.

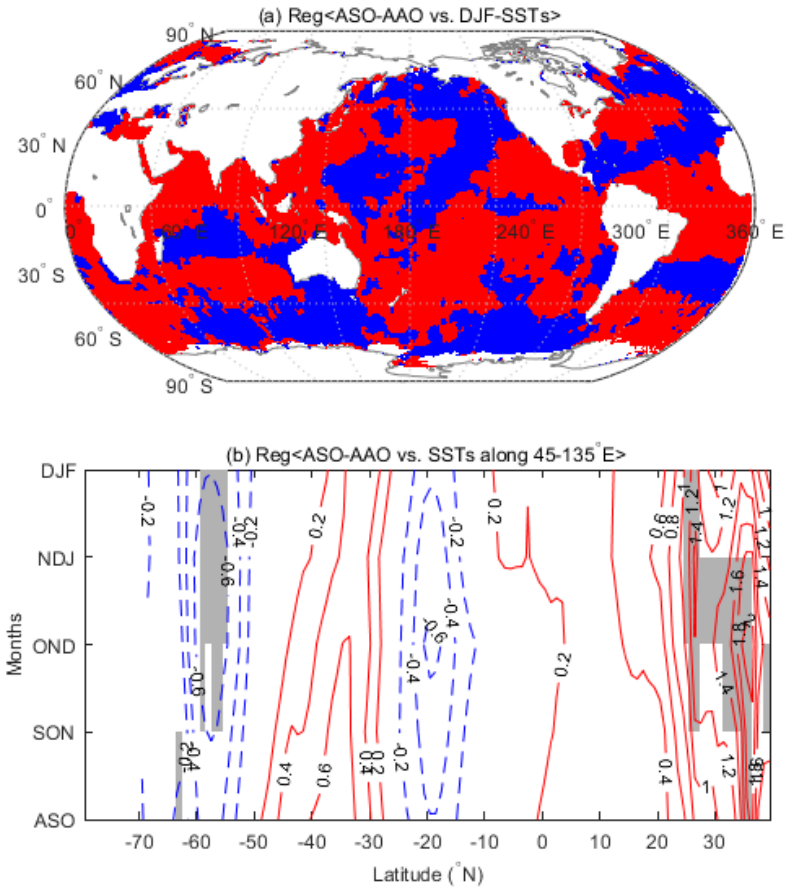

Figure 2 . a Regression coefficients between the ASO-AAO and DJF-SSTs (red shadings indicate positive regression coefficients, blue shadings indicate negative regression coefficients) and b Zonal mean SSTs between 45-135E from ASO to DJF in association with one unit of ASO-AAO index (significant at 90% level are indicated by gray shadings)

2) Changes in ocean heat content caused by AAO variations

Based on the monthly Ocean Reanalysis data (ORAS5), several indices which are related to the marine thermal environment in Southern Indian Ocean. Here, we divided the Southern Indian Ocean into two parts, namely the north of Southern Indian Ocean (NSIO) and the south of Southern Indian Ocean (NSIO) (Figure 3). That's because NSIO is almost surrounded by the mainland, and the south is the open to the Southern Ocean. The generally characteristics of Land-Sea distribution may involve some different variations in the ocean environments.

Firstly, we examined the variations of sea surface temperature (SST), ocean heat content of the upper 300 m (sohtc300) m and 700 m (sohtc300), the depth of 20℃ isotherm (so20chgt) and net downward heat flux (sohefldo) in NSIO and SSIO, respectively. As shown in Figure 4, it can be seen that the SST, sohtc300, sotch700 and so20chgt in both NSIO and SSIO increased gradually during the last four decades, although they also experienced obviously interannual and interdecadal fluctuations. On the contrary, the evolution trends of sohefldo in both NSIO and SSIO decreased significantly. The reducing of sohefldo indicates that the more heat has being absorbed by the ocean. More heat stored in the Indian Ocean must mean that it is warming. This phenomenon may be closely related to global warming.

In order to reduce the possible influence of the low-frequency variations or long-term trends and to examine whether the correspondence between these two time series is stable on an interannual timescale, the high-frequency (<10 yr) correlation of the high-pass-filtered time series was also calculated by using the Butterworth filter. That is say, there are two correlation coefficients for each two time series, namely r1 and r2 for the raw (unfiltered) correlations and the high-frequency correlations, respectively.

The links between the Antarctic Oscillation indices (AAO) and the marine thermal environment variables were examined by using Pearson correlation coefficient. However, the results suggested that, in generally, there are very weak correlations between AAO and SST, sohtc300, sohtc700, so20chgt and sohefldo, as shown in Table 1. For SST, the significant and stable correlations occurred in SON in SSIO area, 0.33, significant at 95% level. For sohtc300 and sohtc700 in SSIO, they correlated negatively with SON-AAO, -0.34 and -0.35, respectively. Combined with so20chgt, it can be concluded that a positive AAO in SON is conducive to a high SST in SSIO, and less heat content in NSIO (Figure 5). Moreover, the response of zonal and meridional velocity of upper Ocean to AAO in SON were examined by using composite analysis.

However, there are very weak signal (Figure 6). Thus, a further research is needed to uncover the possible links between the marine thermal environments in Southern Indian Ocean.

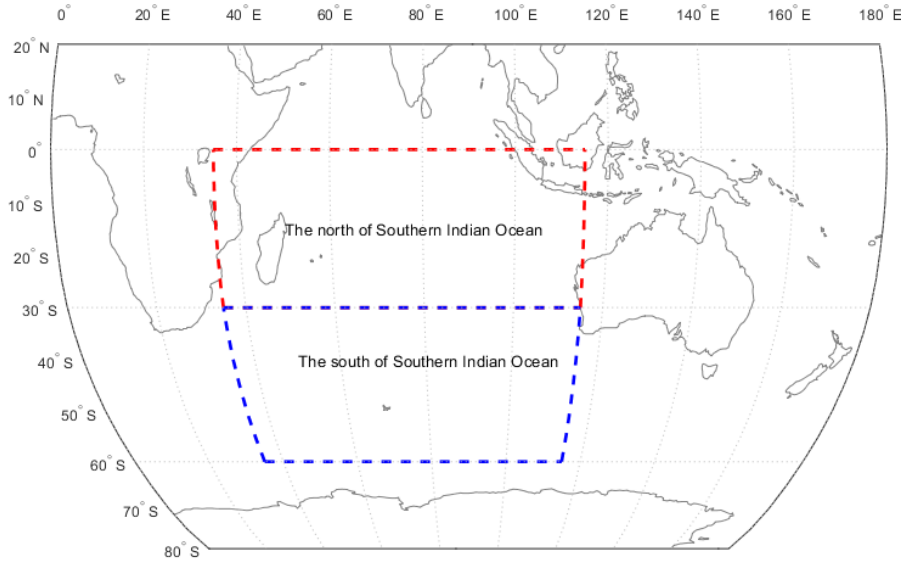

Figure 3. Two parts of Southern Indian Ocean. (NSIO and SSIO denote the north and south of Southern Indian Ocean, respectively)

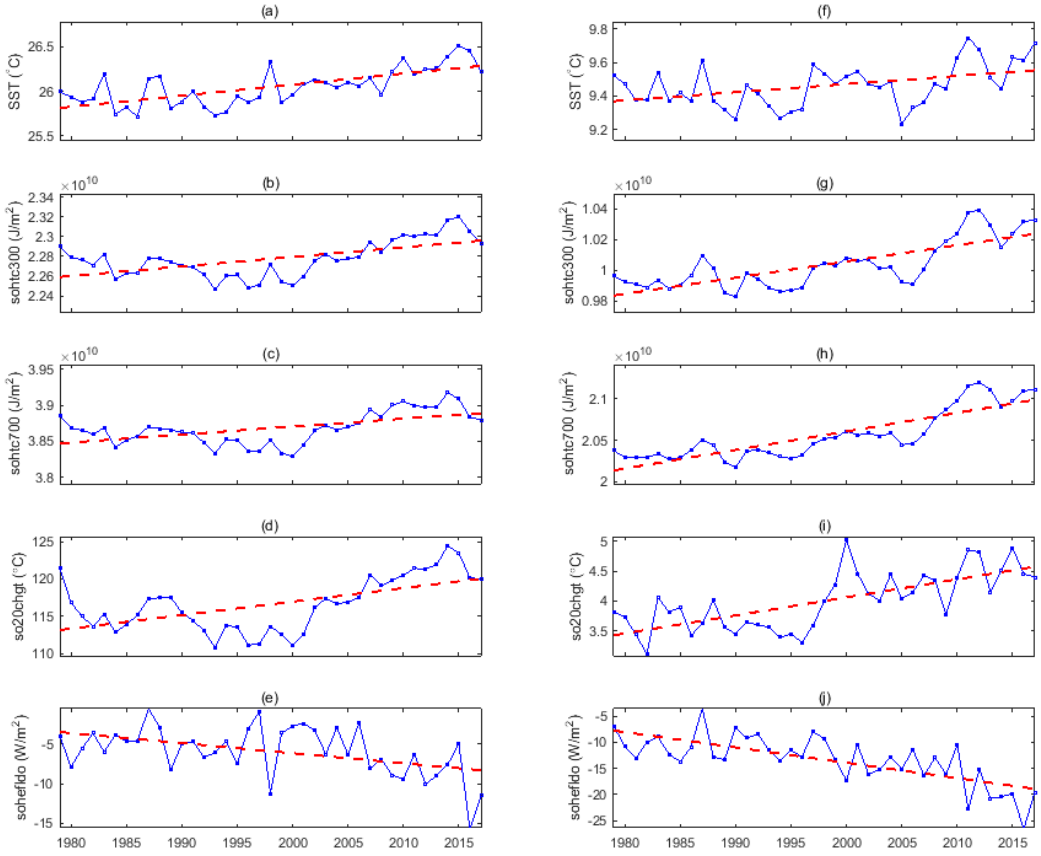

Figure 4. The variations of the annual marine thermal environment in the two parts Southern Indian Ocean

(the sea surface temperature (a, f), ocean heat content of the upper 300 (b, g) and 700 (c, h), depth of 20℃ isotherm (d, i) and the net downward heat flux (e, j) in NSIO (the left panel) and SSIO (the right panel), respectively)

Table 1. List of correlation coefficients between the AAO and the Ocean Heat content related variables in Indian Ocean

		SST		sohtc300		sohtc700		so20chgt		sohefldo	
		NSIO	SSIO	NSIO	SSIO	NSIO	SSIO	NSIO	SSIO	NSIO	SSIO
Annual	r_1	-0.10	0.01	-0.09	-0.14	-0.14	-0.16	-0.10	-0.06	0.28	0.00
	r_2	-0.06	-0.11	-0.06	-0.18	-0.03	-0.14	0.08	0.12	0.34	-0.06
MAM	r_1	0.20	0.22	0.07	0.22	0.03	0.27	0.04	0.21	-0.11	-0.05
	r_2	0.06	0.02	0.03	-0.23	0.03	-0.11	0.08	-0.03	-0.04	0.40
JJA	r_1	0.12	0.29	0.17	0.19	0.12	0.21	0.18	0.30	-0.21	0.01
	r_2	-0.08	0.09	-0.02	-0.07	-0.01	0.05	0.07	0.32	-0.26	0.27
SON	r_1	-0.09	0.26	-0.15	0.14	-0.16	0.09	-0.13	0.02	-0.18	0.10
	r_2	-0.13	0.33	-0.34	0.22	-0.35	0.22	-0.28	0.06	-0.10	0.20
DJF	r_1	0.31	0.14	0.24	0.24	0.22	0.27	0.25	0.15	0.03	-0.15
	r_2	0.06	-0.16	0.14	-0.13	0.06	-0.13	0.11	0.05	0.04	-0.26

Dof = 38, 0.26 and 0.31 for the 90% and 95% significance level, respectively.

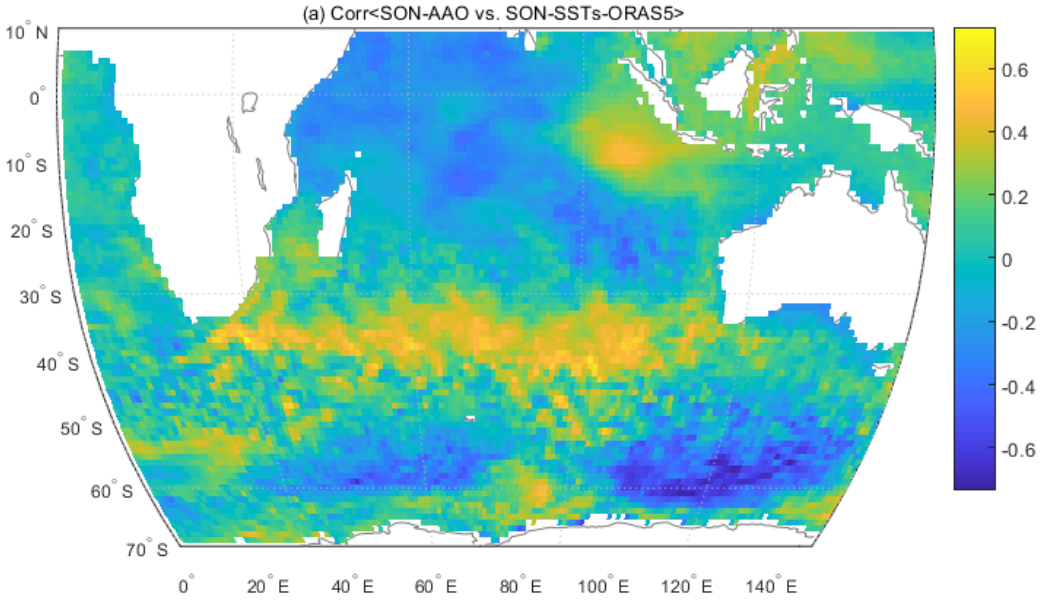

Figure 5. Spatial distribution of high-frequency correlation coefficients between AAO and SSTs in SON

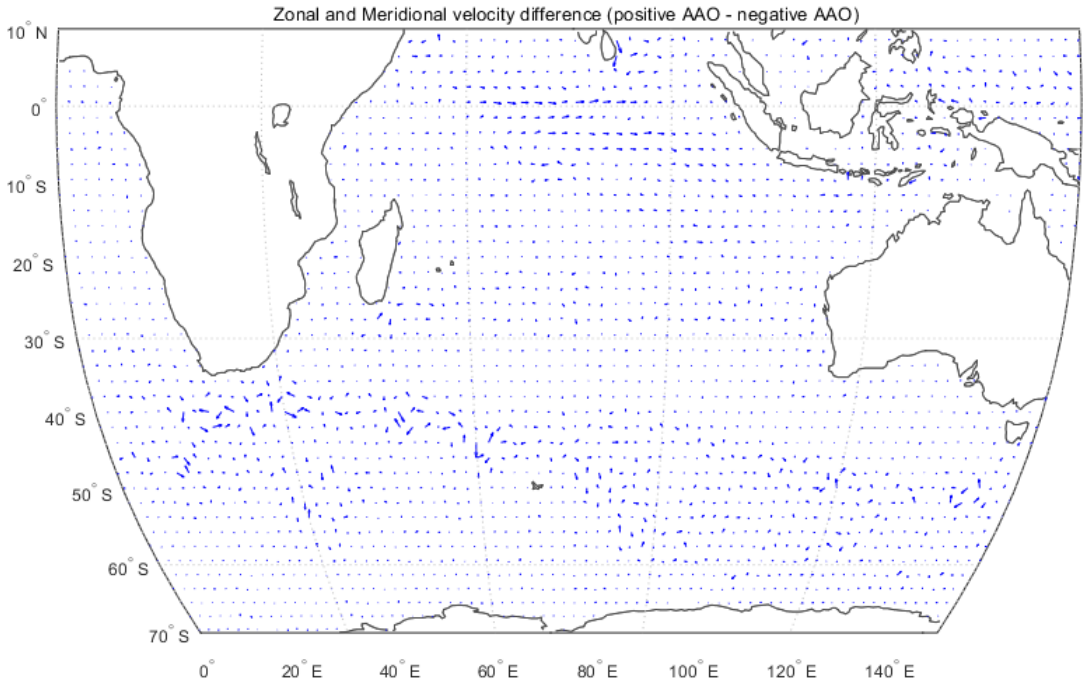

Figure 6. Composite fields of zonal and meridional velocity of upper Ocean according AAO in SON

3) Climatology of wave activity flux during four seasons in the Southern Hemisphere

We firstly examined the climatology of horizontal distribution of wave activities flux and geostrophic streamfunction at 200 hPa during the four austral seasons with the period of 1979-2017 (Figure 7). The wave activity flux is derived by the formula of Takaya & Nakamura (2001). The wave activity flux is at the maximum during the austral summer and autumn by 6 m^2 s^{-1} and at the minimum in the austral spring and winter by 2-3 m^2 s^{-1}. During the austral summer and autumn, the dominant feature of wave activity flux is two wave train pattern in the middle to high latitudes in the Southern Hemisphere indicated by anomalies of geostrophic stream function (GSF). At the high latitudes, the positive GSF anomaly is located over the Weddell Sea and the southern section of the Indian Ocean. The negative anomaly of GSF is located over the Amundsen Sea and the region between 0 and 90E. At the middle latitudes, the wave train is featured by two positive anomalies over the southern section of the Pacific Ocean and the region of 0-90E and two negative ones over the Indian Ocean and the Atlantic ocean. In the austral winter, there is a wave train from the Amundsen Sea eastward to the middle latitude, with a positive anomaly of GSF over the Amundsen Sea and the region between 0 and 90E and a negative anomaly over the southern Section of the Atlantic Ocean. In the austral spring, there is a wave train stretching from the southern Section of the Pacific Ocean across the Antarctic Peninsula and the Atlantic Ocean to the Indian Ocean, with negative GSF anomaly over the Pacific Ocean, Atlantic Ocean and positive ones over the Antarctic Peninsula and the region between 0 and 90E. By comparing the spatial distribution of wave activity flux during the four austral seasons, the wave activity flux is strong at middle latitude during the four austral seasons. Meanwhile, the wave activity flux over the south Pacific Ocean is at the maximum.

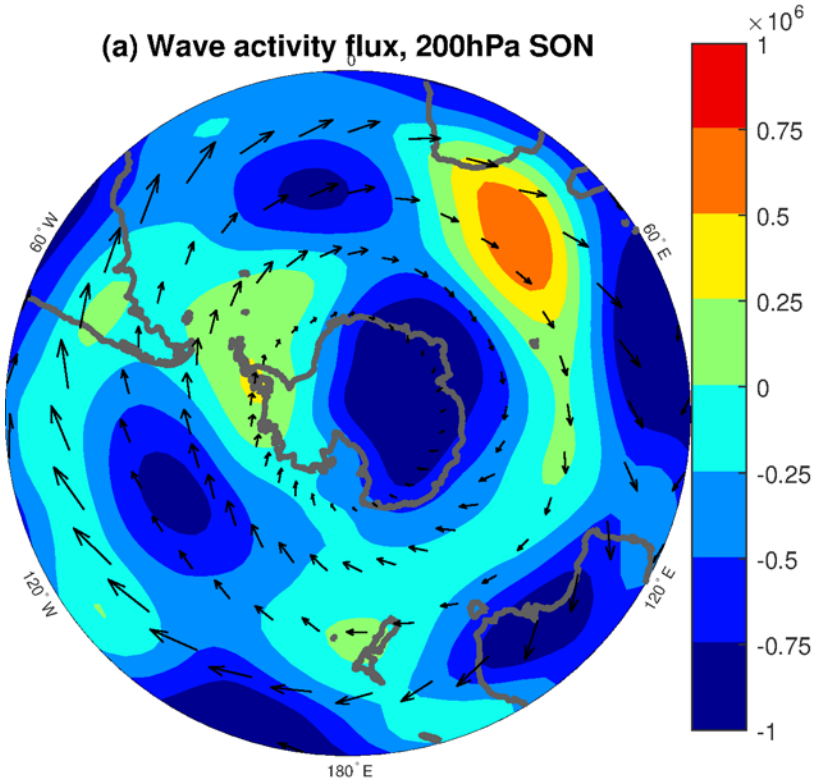
(a) Wave activity flux, 200hPa SON
0
60°W
60°E
120°W
120°E
180°E
×10^6
1
0.75
0.5
0.25
0
-0.25
-0.5
-0.75
-1

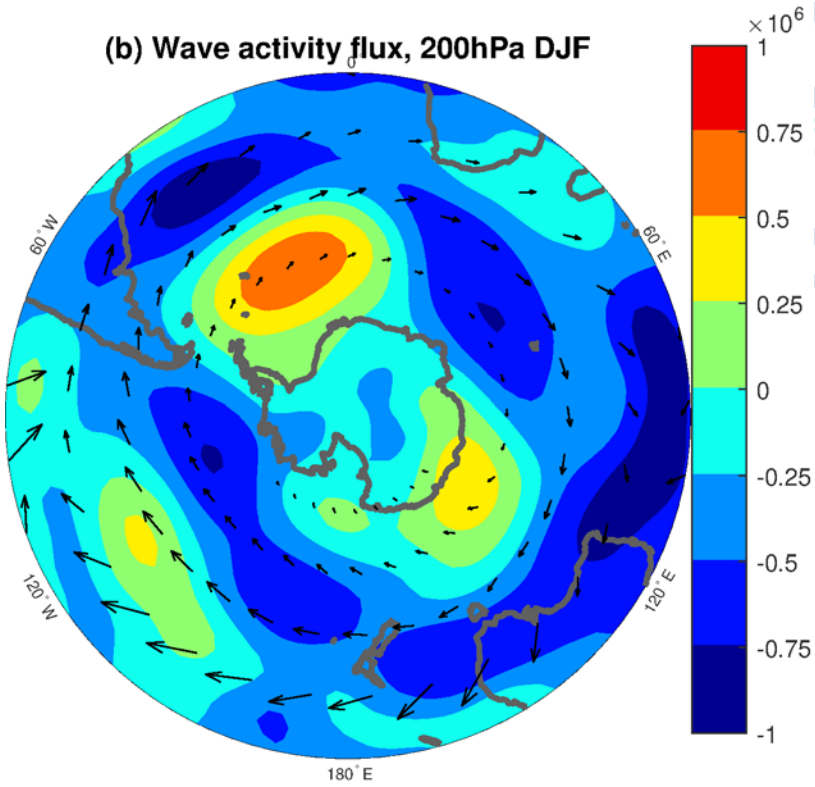
(b) Wave activity flux, 200hPa DJF
0
60°W
60°E
120°W
120°E
180°E
×10^6
1
0.75
0.5
0.25
0
-0.25
-0.5
-0.75
-1

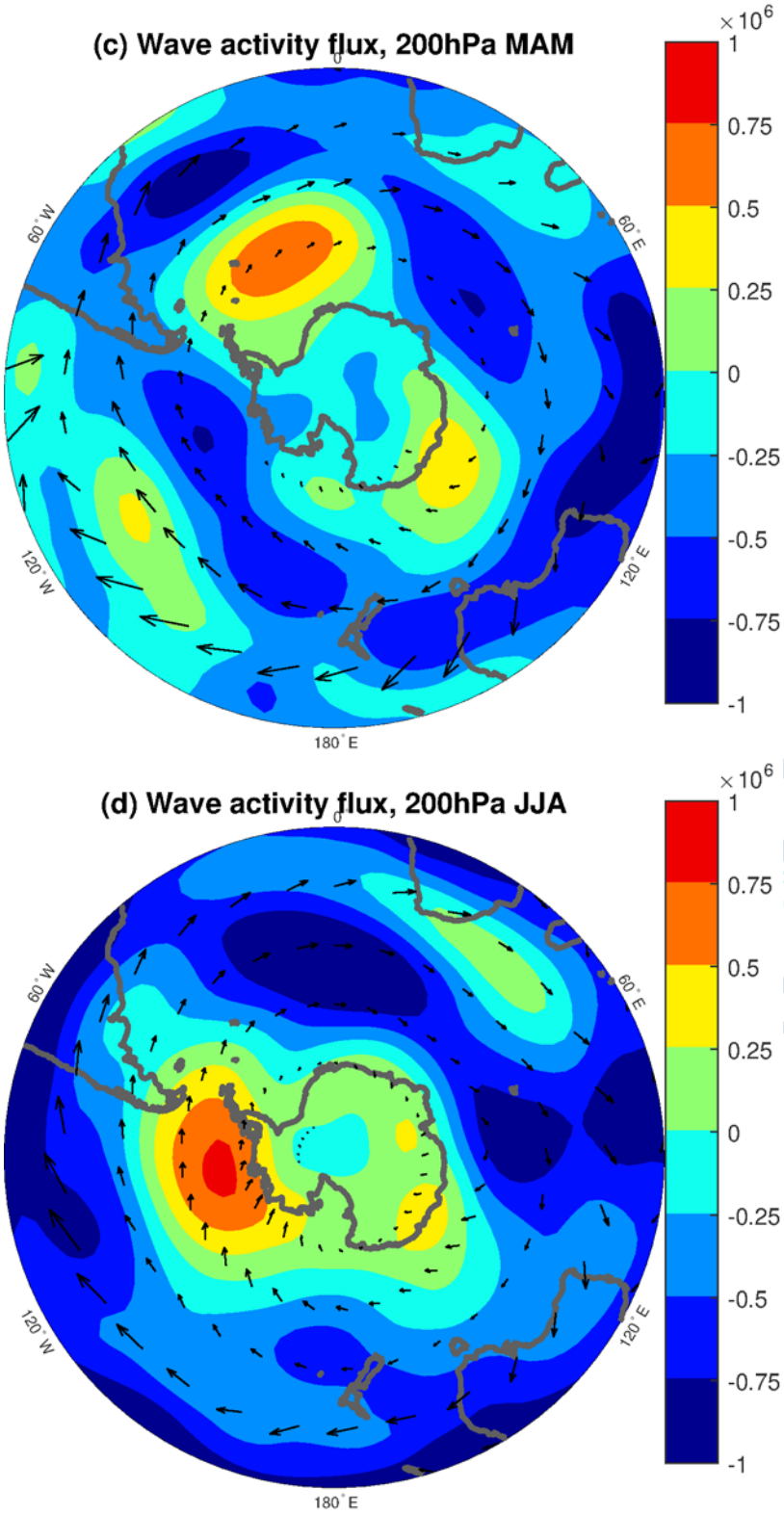

Figure 7. Climatology of wave activity flux and geostrophic streamfunction at 200 hPa during the austral spring (a), summer (b), autumn (d), and winter (d). The geostrophic streamfunction is shaded and horizontal wave activity flux is shown by vectors. The maximum of vector is equal to 3, 6, 6, and 4 m^2s^{-1}.

We then analyzed vertical distribution of wave activity flux and geostrophic streamfunction during four austral seasons. For clarity, we showed those results in the austral summer and winter, respectively. To describe the difference in the wave activity flux and geostrophic streamfunction, we divided the southern Hemisphere into four parts, i.e., 0-90E, 90E-180, 180-90W, and 90W-0. Figure 8 to Figure 11 show the wave activity flux in the austral summer. The geostrophic streamfunction in the region of 0-90E and 180-90W shows negative value across the southern Hemisphere in the middle to high troposphere. However, in the region 90E-180 and 90W-0, the negative geostrophic streamfunction mainly locate at low and high latitudes in the middle to high troposphere. Between these two negative geostrophic streamfunction is positive geostrophic streamfunction in the middle to high troposphere. The vertical wave activity flux is large at middle latitude in the lower troposphere by more than 0.005. The value of vertical wave activity flux decreases with height, with the maximum between 90E and 90W.

The meridional wave activity flux show two different features in the southern Hemisphere. In the region of 90W-90E, meridional wave activity flux is positive from the lower to high troposphere with a center in the high troposphere at middle latitude. However, the meridional wave activity flux show a dipole structure at lower to middle latitude in the middle to high troposphere. In the region of 90E to 90W, The meridional wave activity flux is positive at low latitudes with a center at 250 hPa and is negative at high latitude from the lower to the middle troposphere. It means that wave train in the middle latitude transports to high latitude and low latitude simultaneously in the region from 90E to 90W. In contrast to the region from 90E to 90W, wave train just stretches from the middle latitude to the low latitude in the region from 90W to 90E. The zonal wave activity flux is similar among four subregions in the southern Hemisphere, i.e., positive values at middle latitude from the middle troposphere to high troposphere, with a center at 500 hPa.

We analyzed the vertical profile of climatological wave activity flux and geostrophic streamfunction in the austral winter during 1979-2017 (Figure 12 to Figure 15). The geostrophic streamfunction is positive at high latitude and negative at low to middle latitude in the troposphere. The vertical wave activity flux shows a positive value from surface to high troposphere in the southern Hemisphere, with the largest value in the lower troposphere. The meridional wave activity flux in the austral winter is similar to that in the austral summer, i.e., positive values from 90W to 90E in the troposphere and a dipole structure from 90E to 90W with positive one at low latitude and negative one at middle to high latitude. The zonal wave activity flux shows positive value in the southern Hemisphere during the austral winter, with a center at 500 hPa.

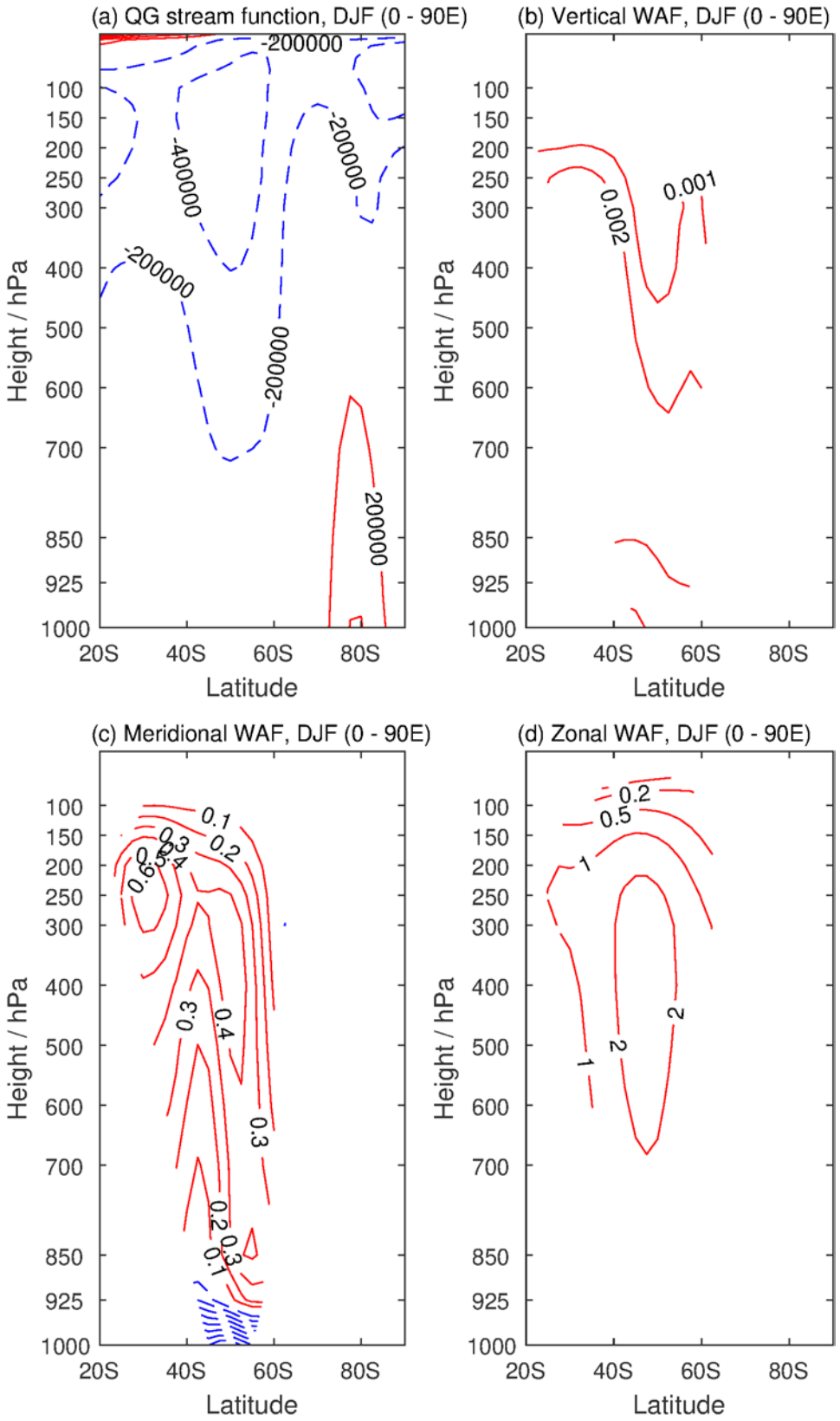

Figure 8. Vertical profile of geostrophic streamfunction (a) and vertical (b), meridional (d) and zonal wave activity flux (WAF) during the austral summer (December to February,DJF) averaged between 0 and 90E in the southern Hemisphere.

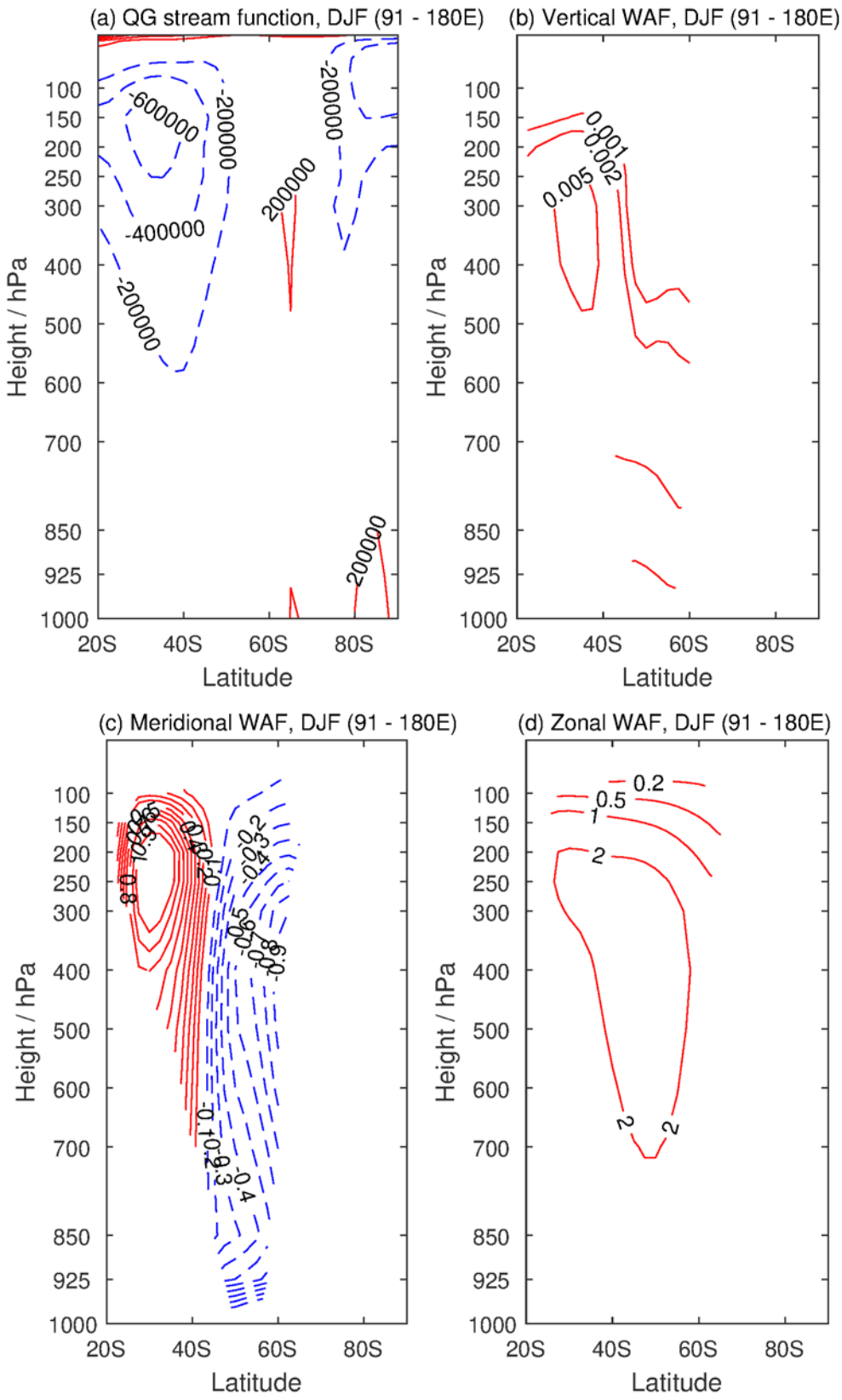

Figure 9. Vertical profile of geostrophic streamfunction (a) and vertical (b), meridional (d) and zonal wave activity flux (WAF) during the austral summer (December to February,DJF) averaged between 90E and 180 in the southern Hemisphere.

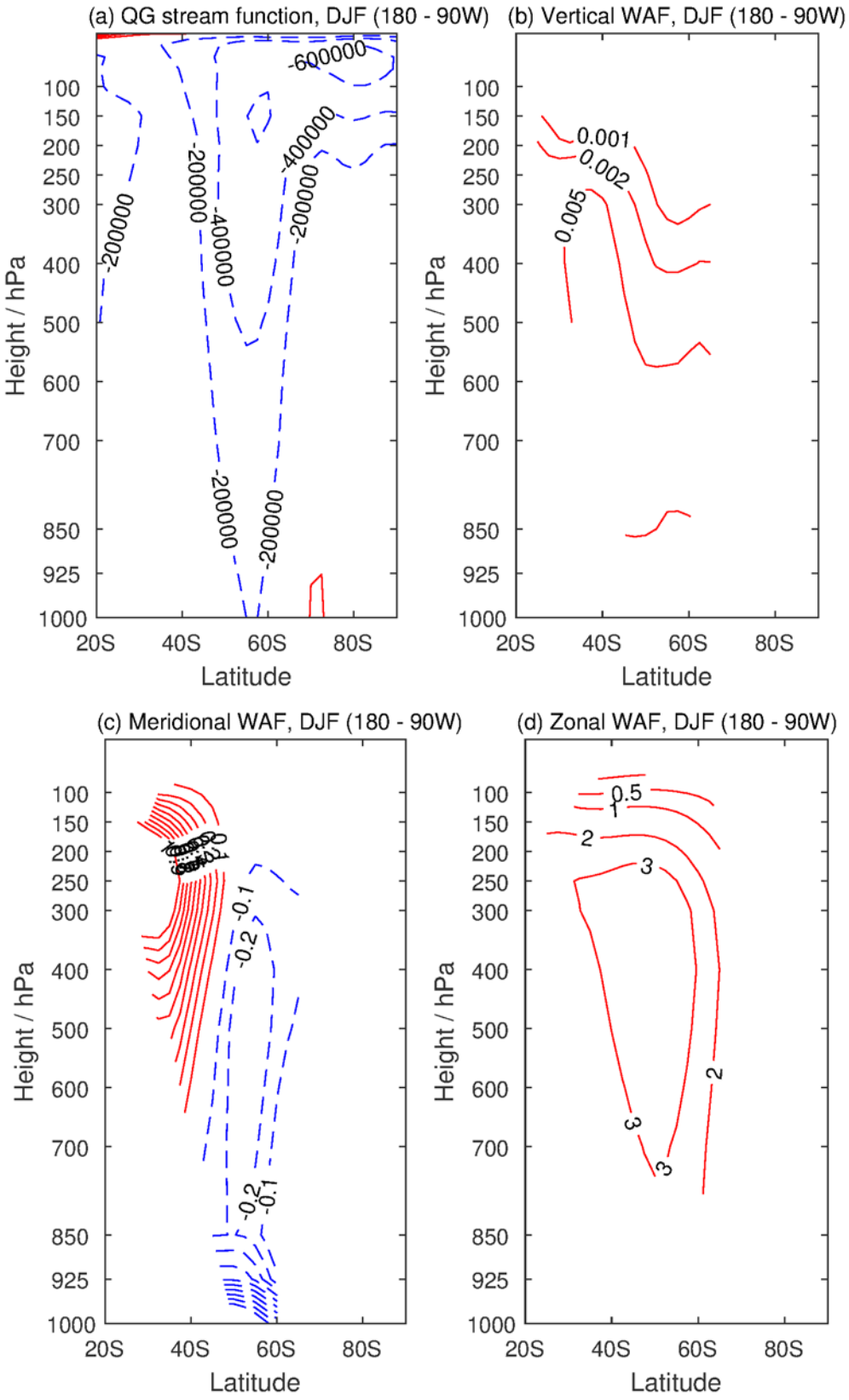

Figure 10. Vertical profile of geostrophic streamfunction (a) and vertical (b), meridional (d) and zonal wave activity flux (WAF) during the austral summer (December to February, DJF) averaged between 180 and 90W in the southern Hemisphere.

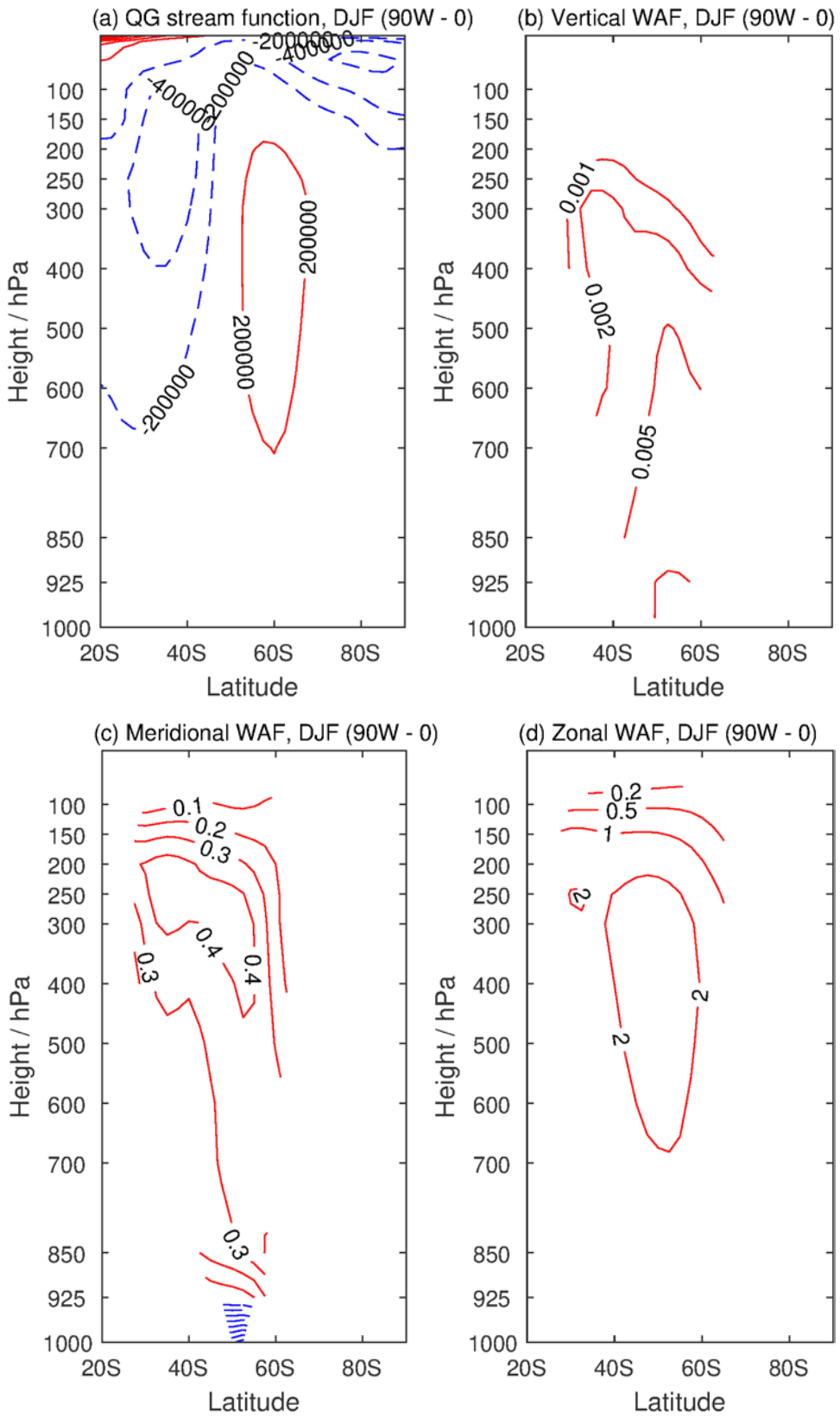

Figure 11. Vertical profile of geostrophic streamfunction (a) and vertical (b), meridional (d) and zonal wave activity flux (WAF) during the austral summer (December to February,DJF) averaged between 0 and 90W in the southern Hemisphere.

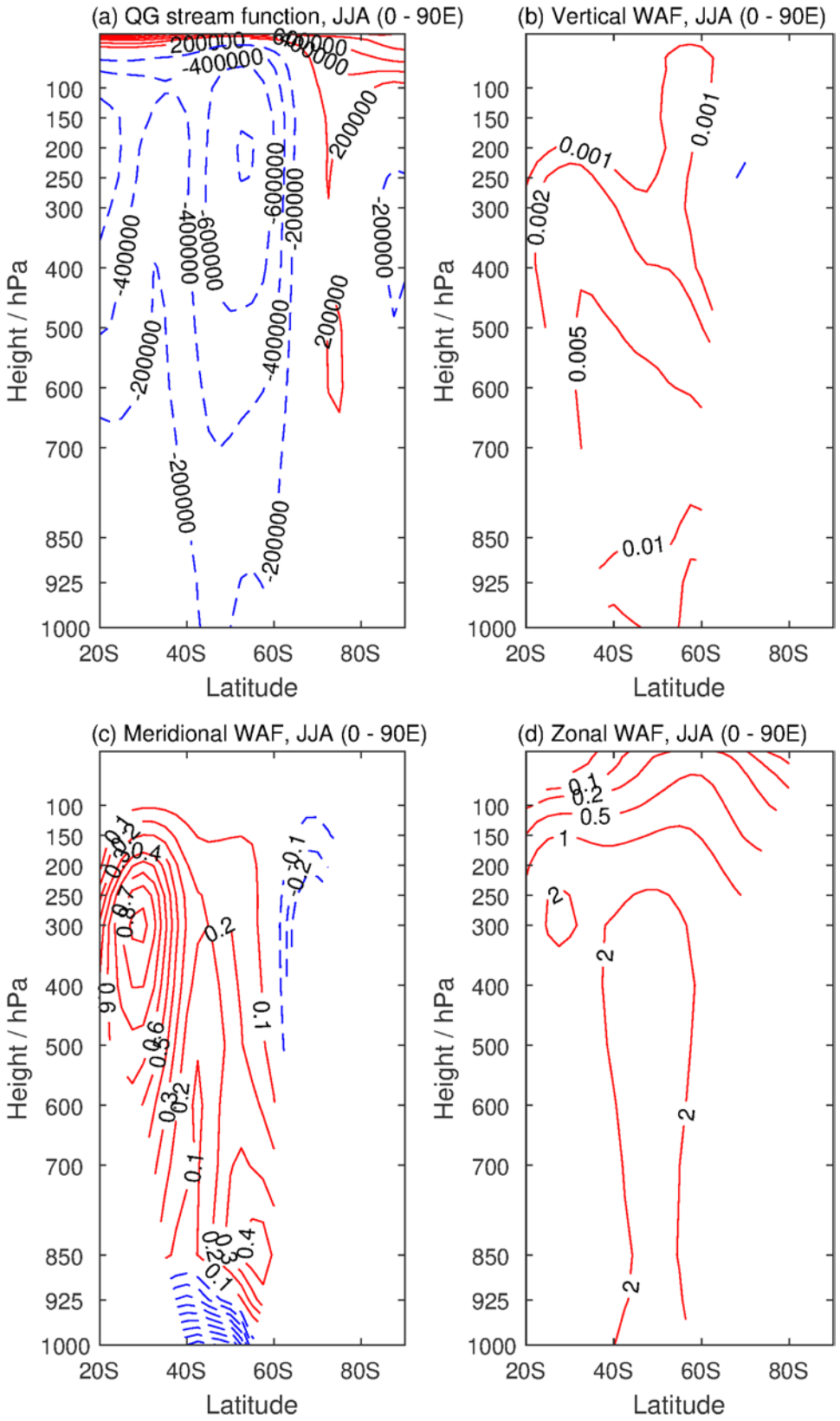

Figure 12. Vertical profile of geostrophic streamfunction (a) and vertical (b), meridional (d) and zonal wave activity flux (WAF) during the austral winter (June to August, JJA) averaged between 0 and 90E in the southern Hemisphere.

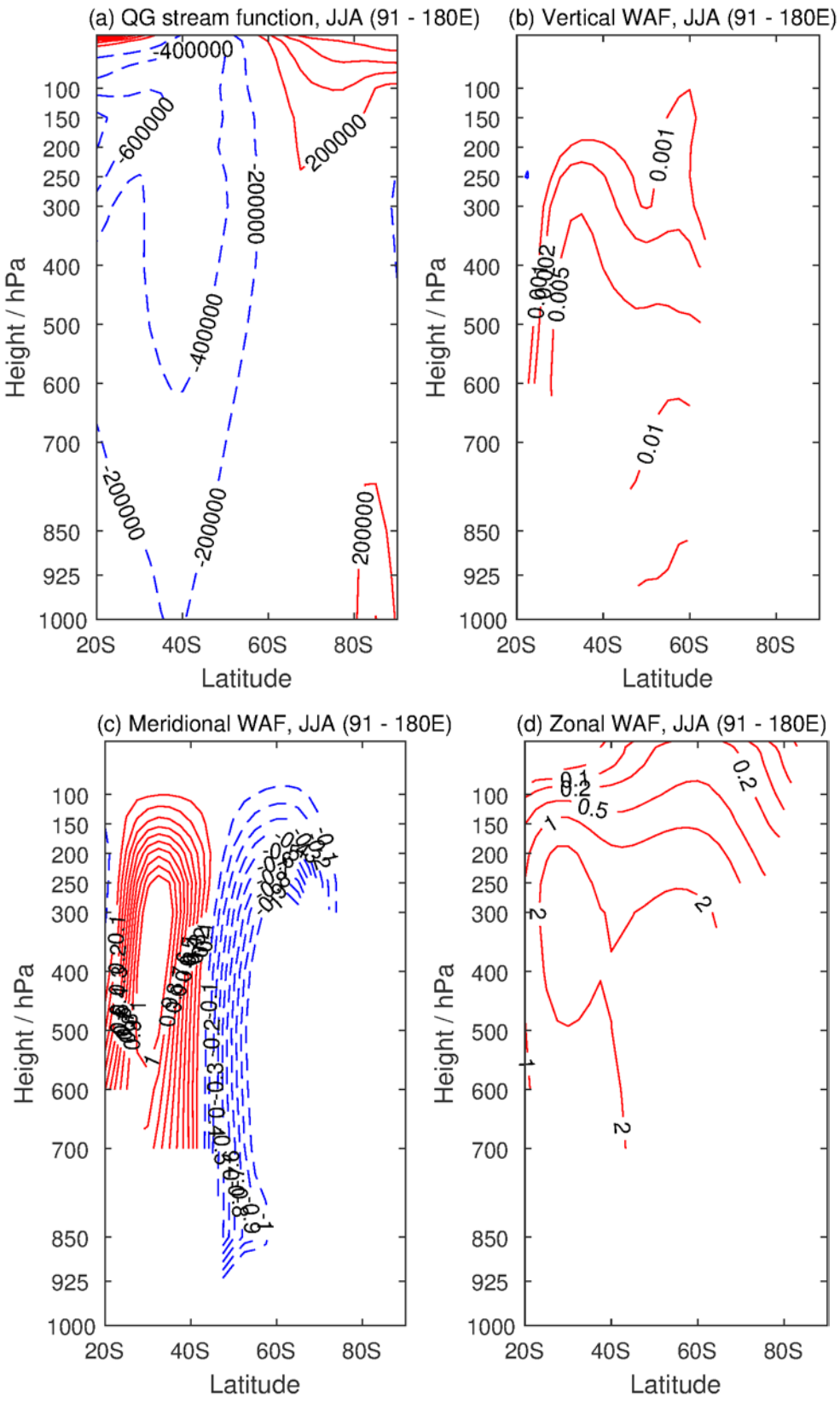

Figure 13. Vertical profile of geostrophic streamfunction (a) and vertical (b), meridional (d) and zonal wave activity flux (WAF) during the austral winter (June to August, JJA) averaged between 90E and 180 in the southern Hemisphere.

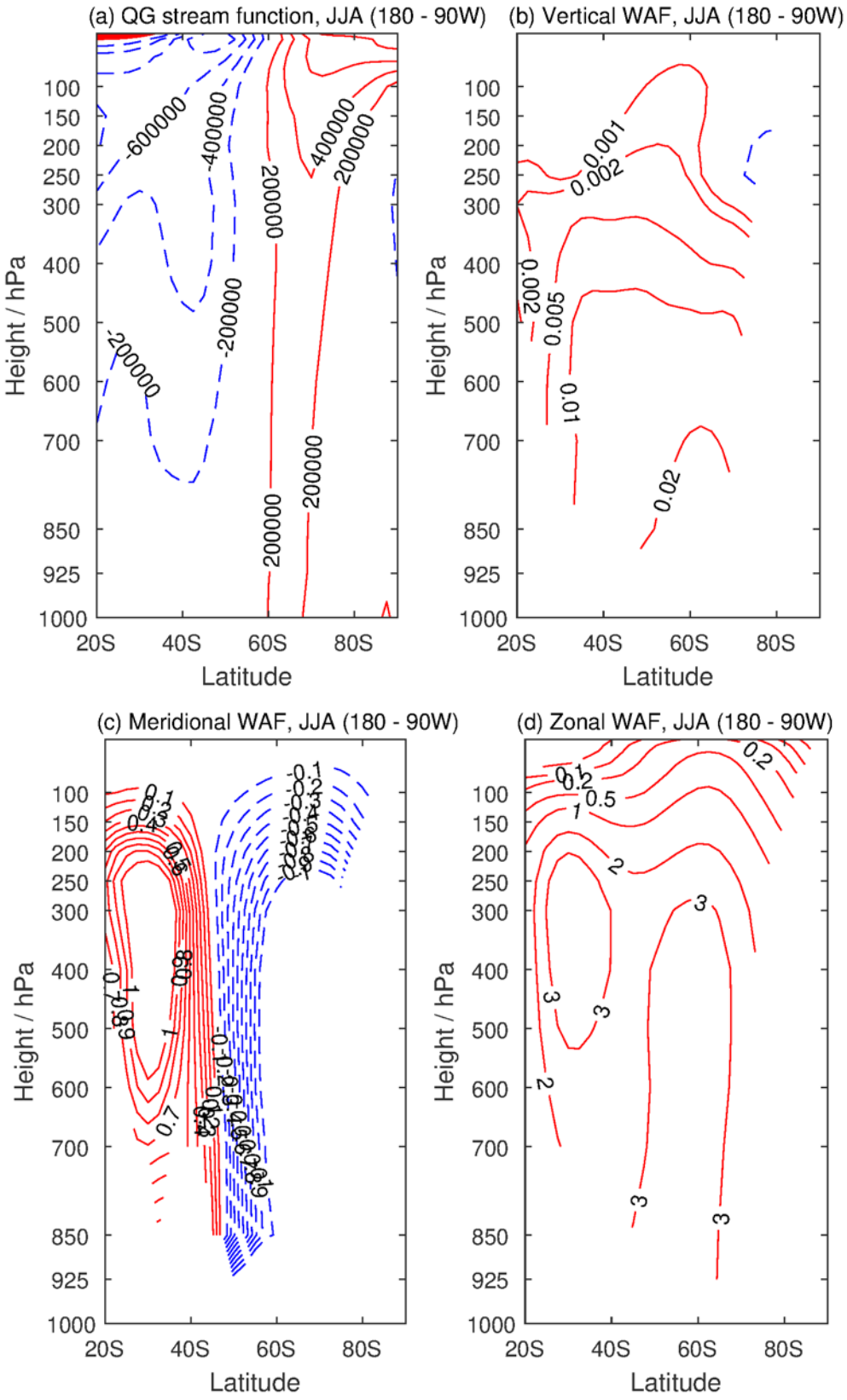

Figure 14. Vertical profile of geostrophic streamfunction (a) and vertical (b), meridional (d) and zonal wave activity flux (WAF) during the austral winter (June to August, JJA) averaged between 180 and 90W in the southern Hemisphere.

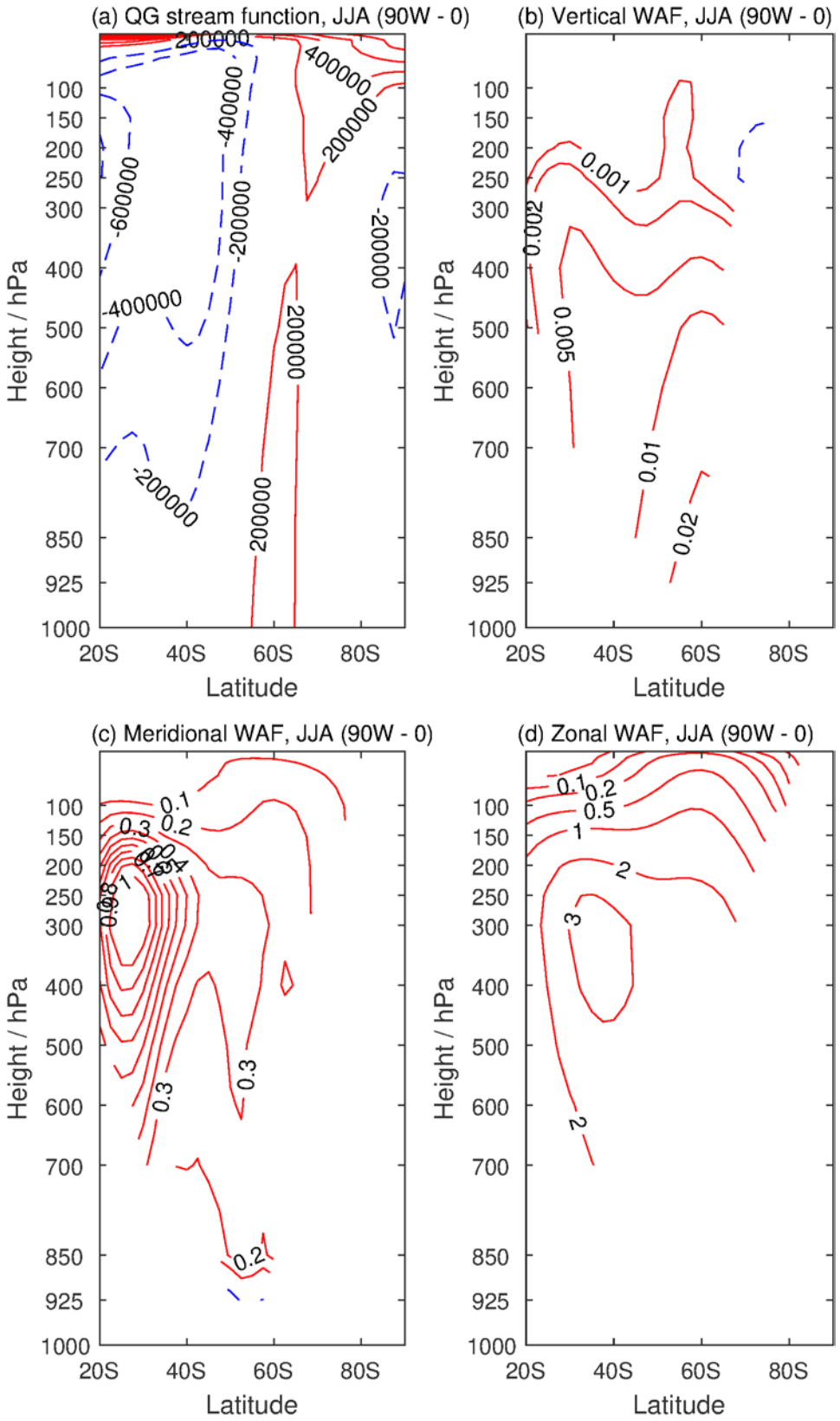

Figure 15. Vertical profile of geostrophic streamfunction (a) and vertical (b), meridional (d) and zonal wave activity flux (WAF) during the austral winter (June to August, JJA) averaged between 0 and 90W in the southern Hemisphere.

4) Changes in the wave activity flux and geostrophic streamfunction caused by AAO variations

To examine the changes in the wave activity flux and geostrophic streamfunction caused by AAO variations, we regressed wave activity flux and geostrophic streamfunction against AAO index in the middle and high troposphere during four austral seasons at an interannual time scale. In the middle troposphere (Figure 16), when the AAO is in a positive phase, the geostrophic streafunction increases over the Antarctica and decreases at middle latitude, with the largest variations in the austral autumn to the following spring. The anomalous negative anomalies are over the south America, the region along 180, and the southern Section of the Indian Ocean in the austral autumn to the following spring. However, the geostrophic streamfunction in the austral summer decreases weaker compared to other seasons with a center over the southern Section of the Pacific Ocean.

The regression of horizontal wave activity flux against the AAO variations at 200 hPa shows different pattern among the four seasons. In the austral spring, when the AAO is in a positive phase, the wave activity from the middle latitude to low latitude increases over the southern section of the Pacific Ocean and over the south of South America. In the austral summer and autumn, the eastward wave activity weakens in a positive AAO phase. The horizontal wave activity over the southern Section of the Pacific Ocean decreases. However, in the austral winter, the wave activity from the middle latitude to high latitude increases over the southern Section of the Pacific Ocean and the Indian Ocean.

The changes in the wave activity flux and geostrophic streamfunction caused by AAO variations at 500 hPa level are similar to those at 200 hPa (Figure 17). When the AAO is in a positive phase, the geostrophic streafunction increases over the Antarctica and decreases at middle latitude during the four seasons. The anomalous negative anomalies are at middle latitude and the positive anomaly of geostrophic streamfunction is over the Antarctica. The geostrophic streamfunction in the austral summer decreases weaker compared to other seasons with a center over the southern Section of the Pacific Ocean. The regression of horizontal wave activity flux against the AAO variations at 500 hPa shows decreased wave activity in the austral summer and autumn at middle latitude. In the austral winter, the wave activity from the middle latitude to high latitude increases over the southern Section of the Pacific Ocean and the Indian Ocean.

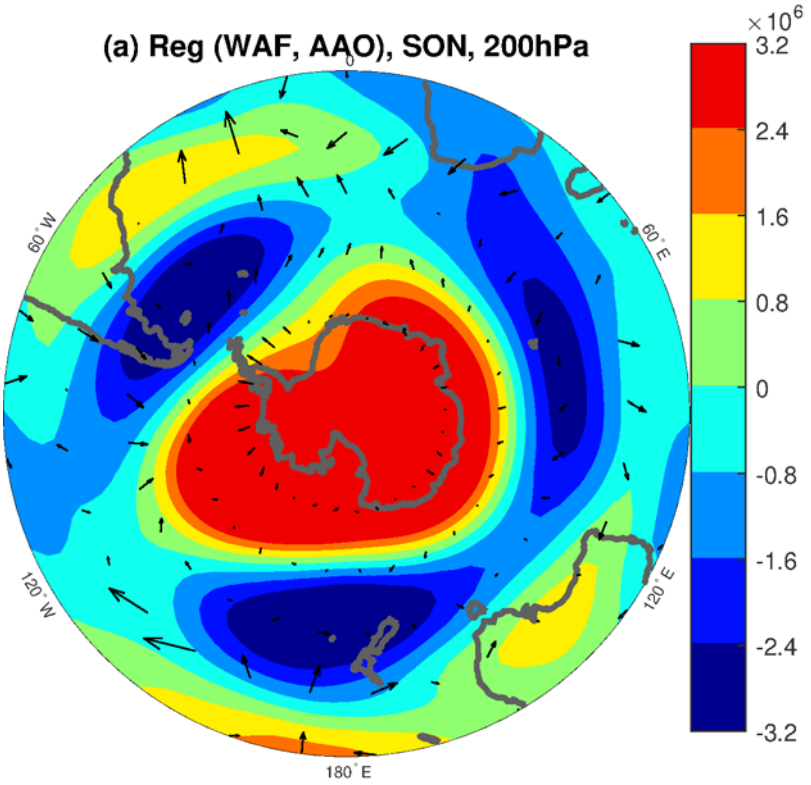
(a) Reg (WAF, AAO), SON, 200hPa
0
60˚W
60˚E
120˚W
120˚E
180˚E
×10^6
3.2
2.4
1.6
0.8
0
-0.8
-1.6
-2.4
-3.2

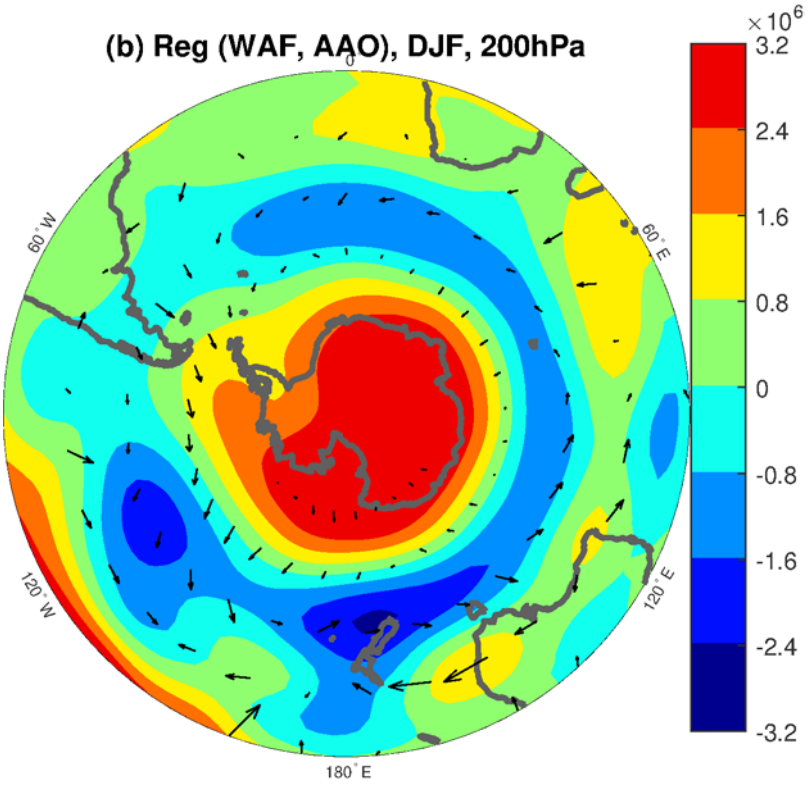
(b) Reg (WAF, AAO), DJF, 200hPa
0
60˚W
60˚E
120˚W
120˚E
180˚E
×10^6
3.2
2.4
1.6
0.8
0
-0.8
-1.6
-2.4
-3.2

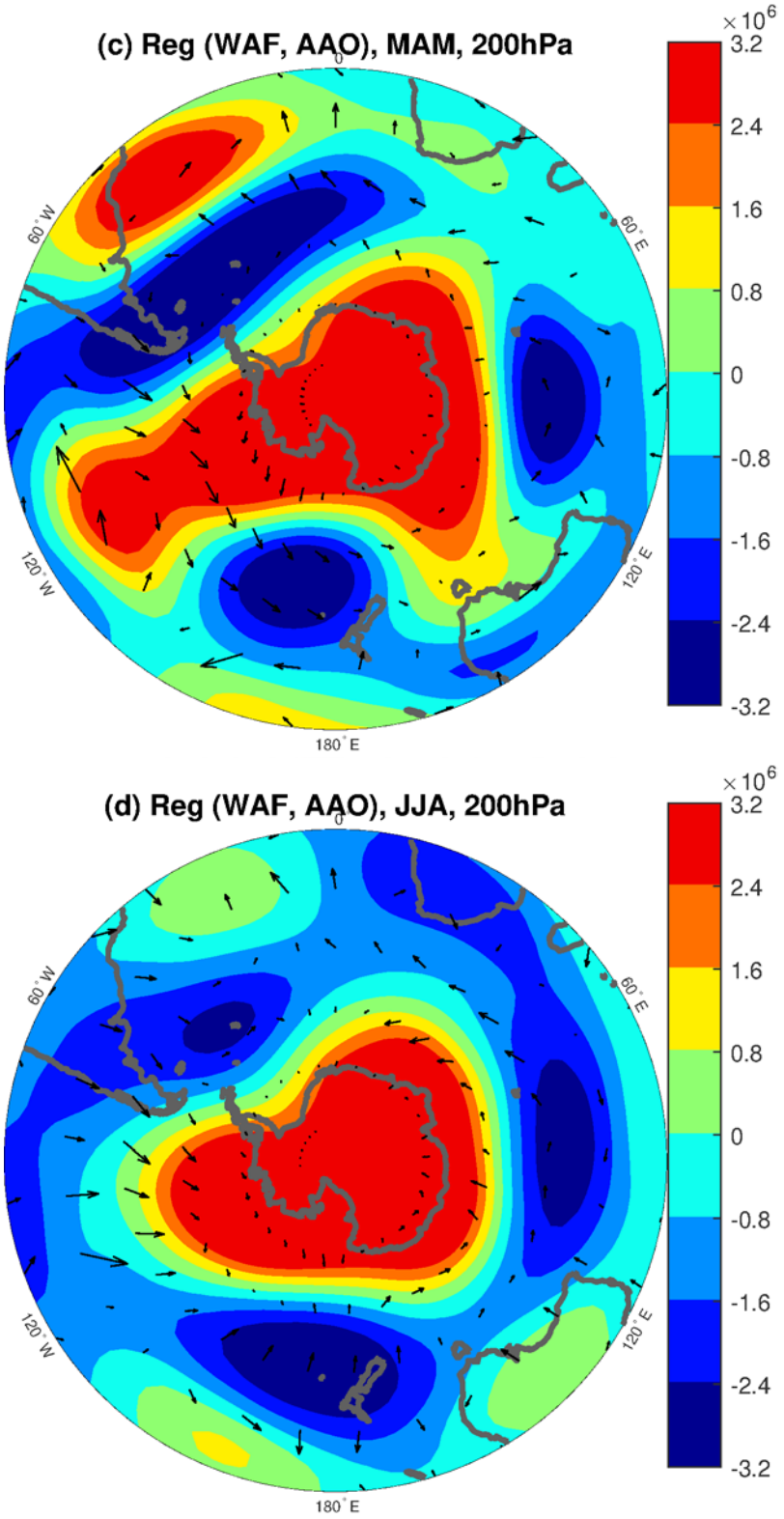

Figure 16. Regression of horizontal wave activity flux and geostrophic streamfunction at 200 hPa level against Antarctic Oscillation index at an interannual timescale during the austral spring (a), summer (b), autumn (d), and winter (d).

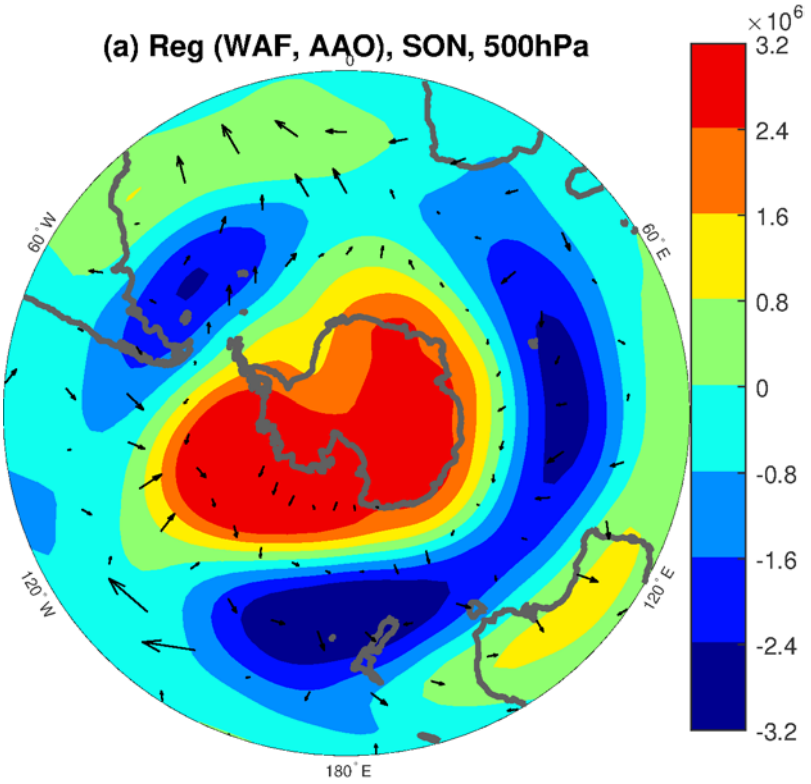
(a) Reg (WAF, AAO), SON, 500hPa
0
60°W
60°E
120°W
120°E
180°E
×10^6
3.2
2.4
1.6
0.8
0
-0.8
-1.6
-2.4
-3.2

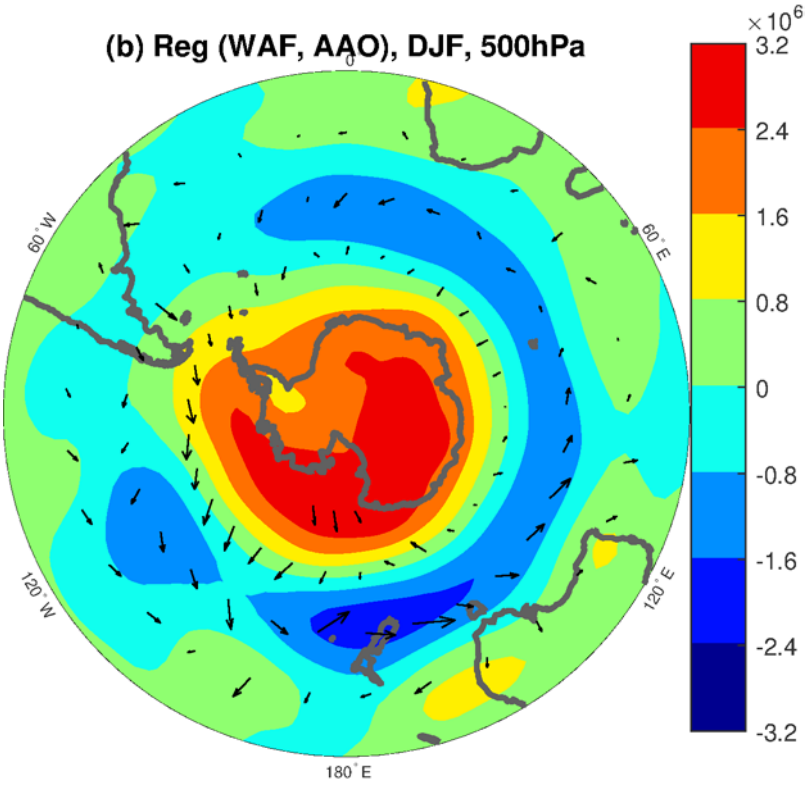
(b) Reg (WAF, AAO), DJF, 500hPa
0
60°W
60°E
120°W
120°E
180°E
×10^6
3.2
2.4
1.6
0.8
0
-0.8
-1.6
-2.4
-3.2

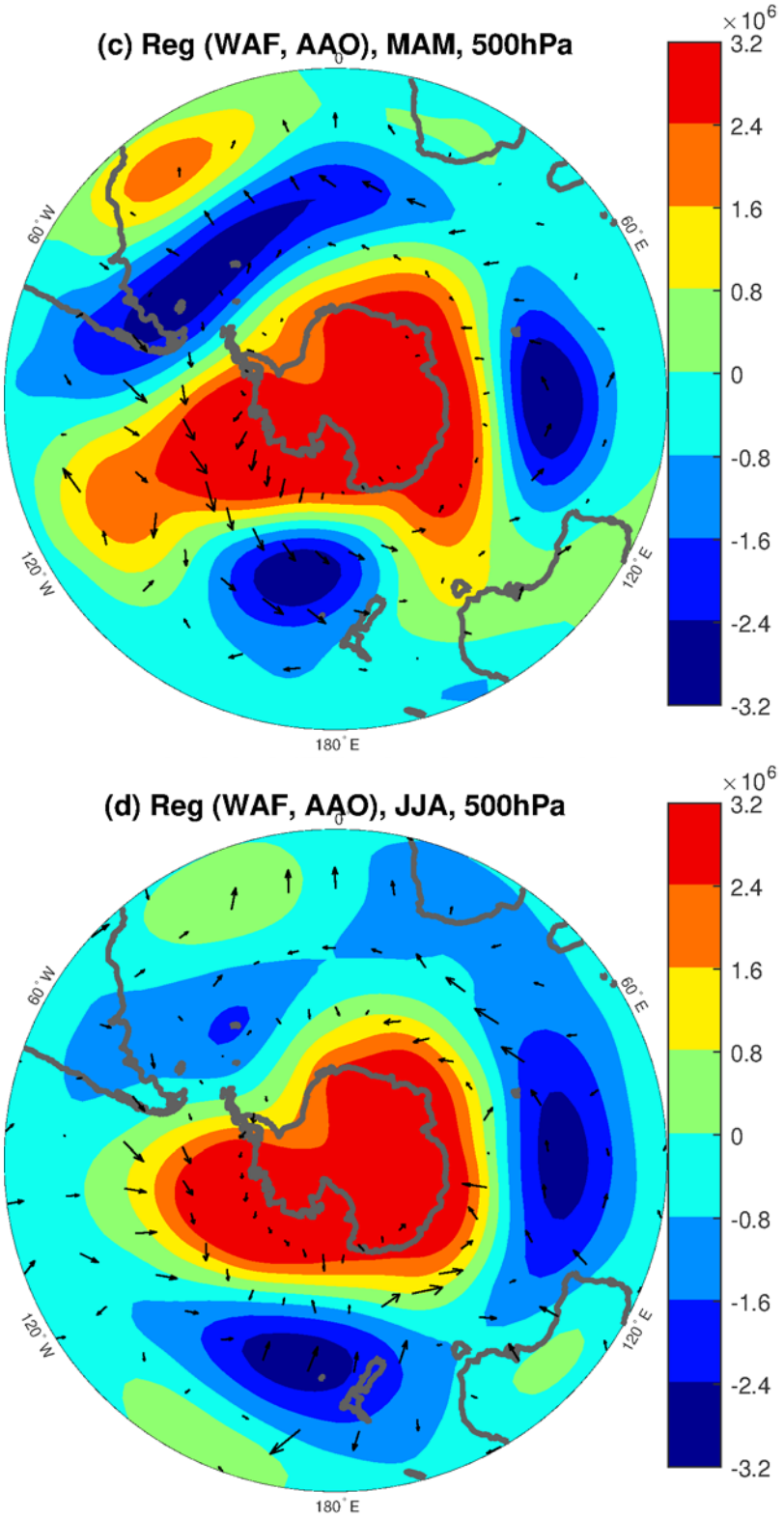

Figure 17. Regression of horizontal wave activity flux and geostrophic streamfunction at 200 hPa level against Antarctic Oscillation index at an interannual timescale during the austral spring (a), summer (b), autumn (d), and winter (d).

5) The relationship between AAO and moisture over tropical Indian-Pacific Ocean

To identify the relationship between AAO and moisture over tropical Indian-Pacific Ocean, the AAO-associated relative humidity and specific humidity in the lower-troposphere during boreal winter (December-January-February), spring (March-April-May), summer (June-July-August) and autumn (September-October-November) were investigated (Figure 18and Figure 19). The common feature of all seasons are the increasing relative humidity and specific humidity over Australia and its surrounding maritime area during the positive phase of AAO.

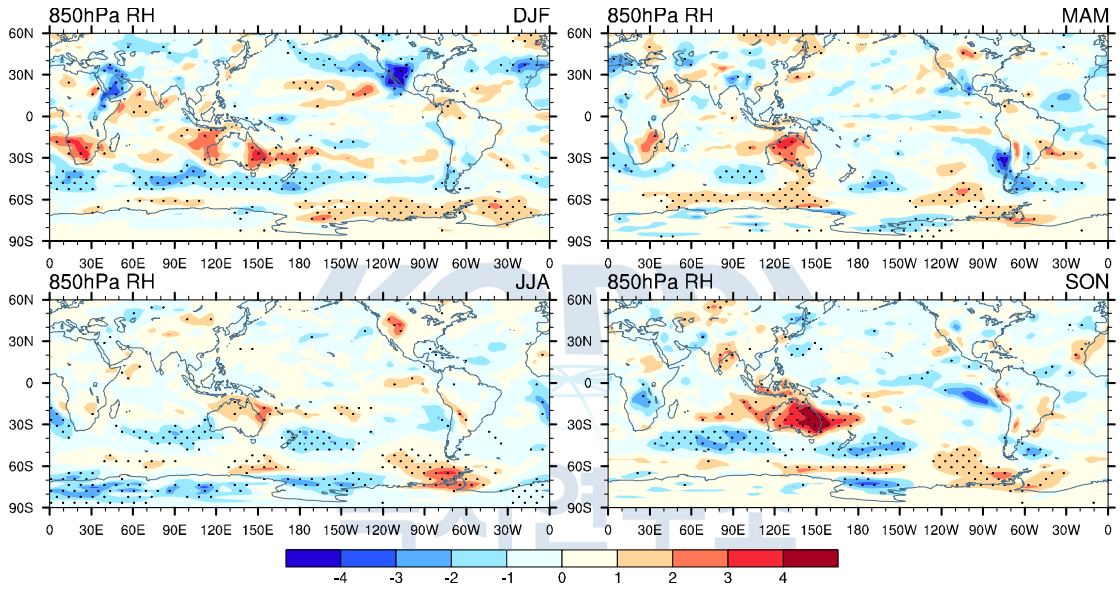

Figure 18. Detrended 850hPa relative humidity (%) regressed to AAO in DJF, MAM, JJA and SON, respectively. The black dots indicate results are significant at 90% confidence level.

During boreal spring (MAM) and summer (JJA), specific humidity increases over northern Australia-Tasman Sea related with AAO. But the most significant signals over tropical Indian-Pacific Ocean occurs in boreal winter (DJF). Associated with AAO, there is a zonal dipole specific humidity anomalies over tropical Pacific Ocean, including a triangle area with decreasing specific humidity over central tropical Pacific and a K-shape area with increasing specific humidity over western tropical Pacific. In contrast, significant specific humidity anomalies appear over South Asia and tropical southeastern Indian Ocean-Australia-Tasman Sea, while negative anomalies occur over western North Pacific Ocean in boreal autumn (SON).

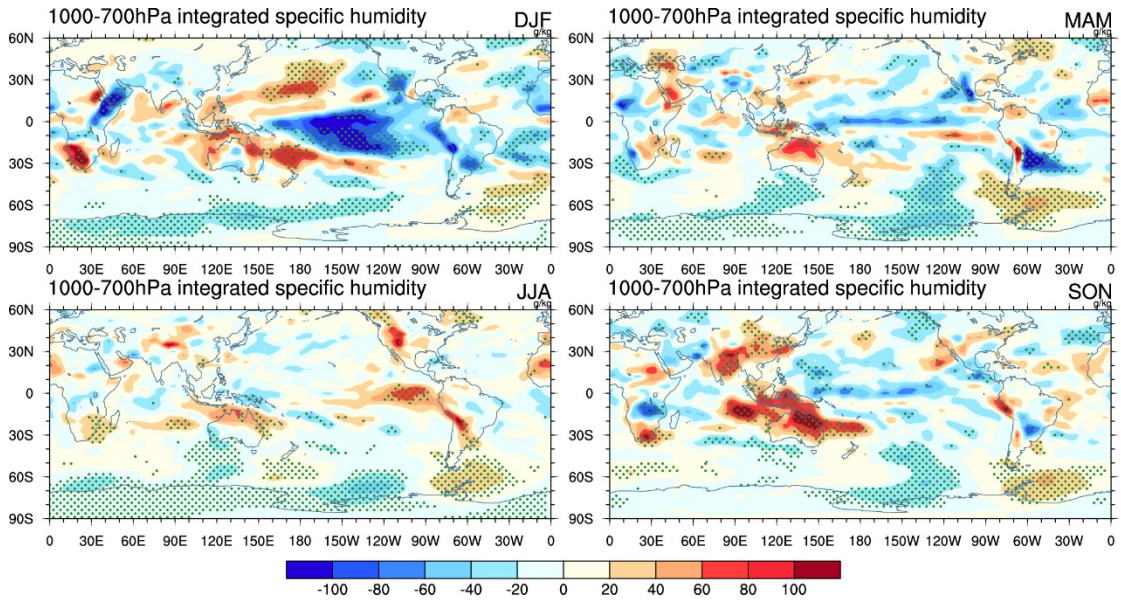

Figure 19. Detrended 1000-700hPa vertical integrated specific humidity (g/kg) regressed to AAO in DJF, MAM, JJA and SON, respectively. The green dots indicate results are significant at 90% confidence level.

To understand how the AAO remarkably influences relative humidity and specific humidity over tropical Indian-Pacific Ocean in boreal winter and autumn, we further calculated AAO-associated atmospheric circulation, moisture fluxes and moisture flux convergence in the lower troposphere (Figure 20 and Figure 21). In boreal winter, the zonal dipole specific humidity should be attributed to the AAO-related high pressure anomalies over eastern North and South Pacific Ocean accompanied with a pair of equatorial symmetric anti-cyclones. The westward moisture fluxes induced by low-level atmospheric circulation lead to the moisture convergence and divergence over western and central tropical Pacific Ocean, respectively.

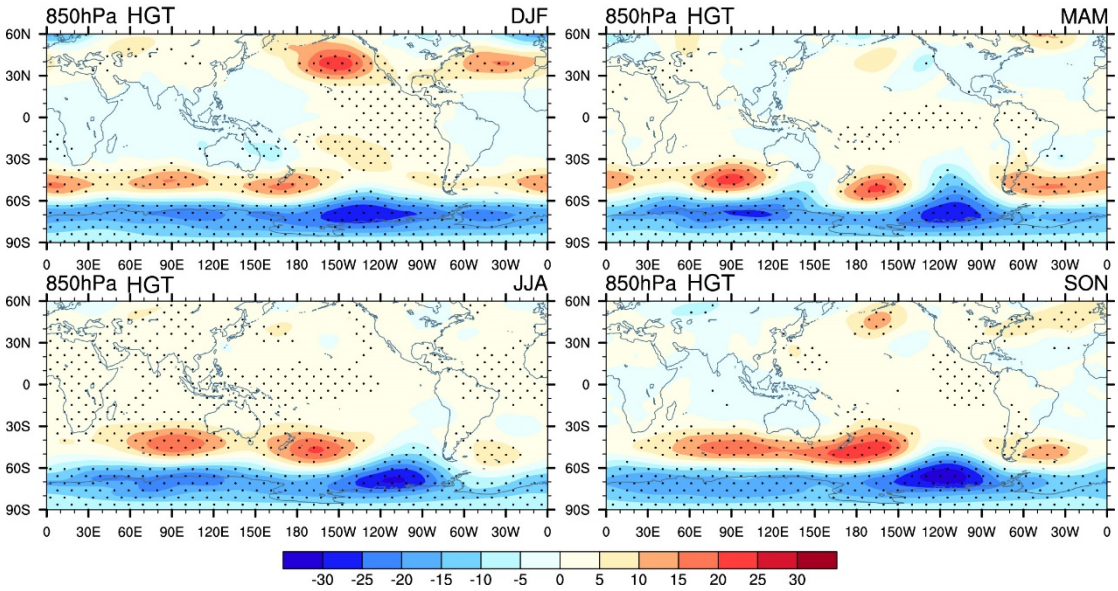

Figure 20. Detrended 850hPa geopotential height (gpm) regressed to AAO in DJF, MAM, JJA and SON, respectively. The black dots indicate results are significant at 90% confidence level.

Similarly, positive geopotential height anomalies induced by AAO occur over western Pacific Ocean in boreal autumn. Two anomalous anti-cyclones transport moisture from central tropical Pacific to western Pacific and coastal areas over southeastern China and northeastern Australia, which cause increasing specific humidity over South Asia and tropical southeastern Indian Ocean-Australia-Tasman Sea and decreasing specific humidity over western North Pacific Ocean.

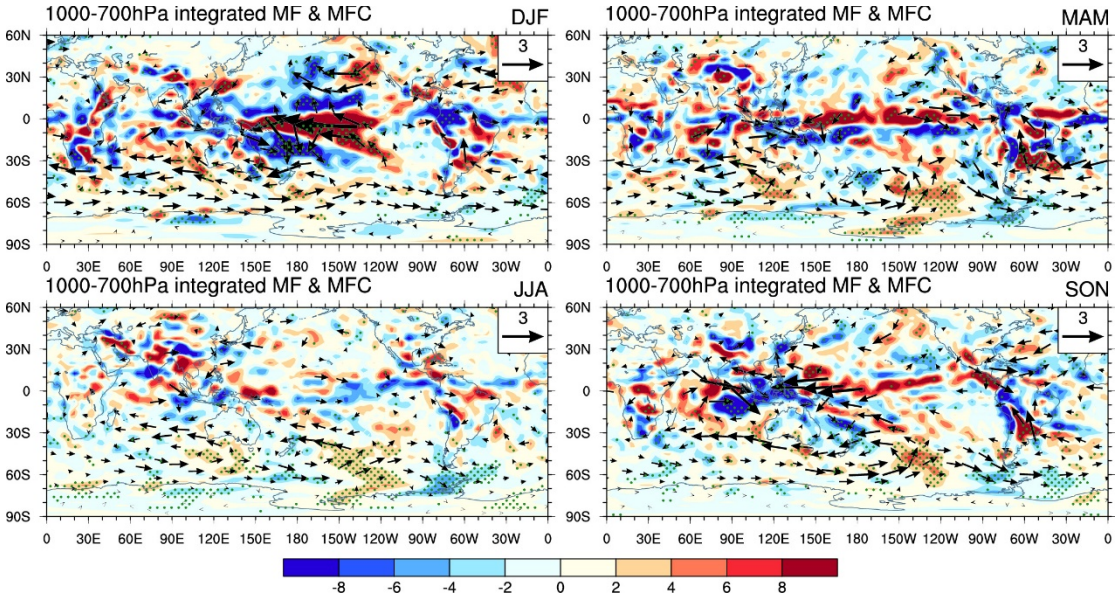

Figure 21. Detrended 1000-700hPa integrated moisture fluxes (vectors: $10^{3}g{\cdot}s^{-1}{\cdot}hPa^{-1}{\cdot}cm^{-1}$) and moisture flux convergence (shading: $10^{-4}g{\cdot}s^{-1}{\cdot}hPa^{-1}{\cdot}cm^{-2}$) regressed to AAO in DJF, MAM, JJA and

SON, respectively. Only the moisture fluxes significant at 90% confidence level are shown and the green dots indicate the moisture flux divergence are significant at 90% confidence level.

6) The evaluation of Amundsen Sea Low simulated by CMIP5 and CMIP6 models

Amundsen Sea Low (ASL) is a dynamic climatological low pressure system located in the Pacific sector of the Southern Ocean (Figure 22a), which plays a crucial role in Antarctica climate variation and sea ice production. The realistic simulation of ASL is necessary for the prediction and projection of Antarctica climate. Based on characteristics of ASL, the performance of ASL was comprehensively evaluated in the 11 CMIP5 models and their CMIP6 versions and high-resolution CAS FGOALS-f2 model (Table 2). Both the absolute and relative strength of ASL were analyzed. In general, both of CMIP5 and CMIP6 multi-model ensembles (MME) could roughly reproduce the spatial distribution of ASL with weaker intensity (Figure 22 and Figure 23). The obvious eastward shift of the ASL center from austral summer to winter are also captured by CMIP models.

Table 2. A brief description of CMIP5 and CMIP6 models used in this study

Models		**Institute, Country**
CMIP5	**CMIP6**	
BCC-CSM1-1	BCC-CSM2-MR	Beijing Climate Center, China Meteorological Administration, China
IPSL-CM5A-LR	IPSL-CM6A-LR	Pierre Simon Laplace Institute, France
CESM1-WACCM	CESM2-WACCM	Community Earth System Model Contributors, USA
CanESM2	CanESM5	Canadian Centre for Climate Modelling and Analysis, Canada
MIROC5	MIROC6	Atmosphere and Ocean Research Institute (The University of Tokyo), National Institute for Environmental Studies, and Japan Agency for Marine-Earth Science and Technology, Japan
GFDL-ESM2M	GFDL-ESM4	National Oceanic and Atmospheric Administration, Geophysical Fluid Dynamics Laboratory, USA
MRI-ESM1	MRI-ESM2-0	Meteorological Research Institute, Japan
MPI-ESM-MR	MPI-ESM1-2-HR	Max Planck Institut für Informatik, Germany
GISS-E2-H	GISS-E2-1-H	National Aeronautics and Space Administration- Goddard Institute for Space Studies, USA
NorESM1-M	NorESM2-LM	Bjerknes Centre for Climate Research, Norwegian Meteorological Institute, Norway
/	CAS FGOALS-f2	State Key Laboratory of Numerical Modeling for Atmospheric Sciences and Geophysical Fluid Dynamics, Institute of Atmospheric Physics, Chinese Academy of Sciences, China

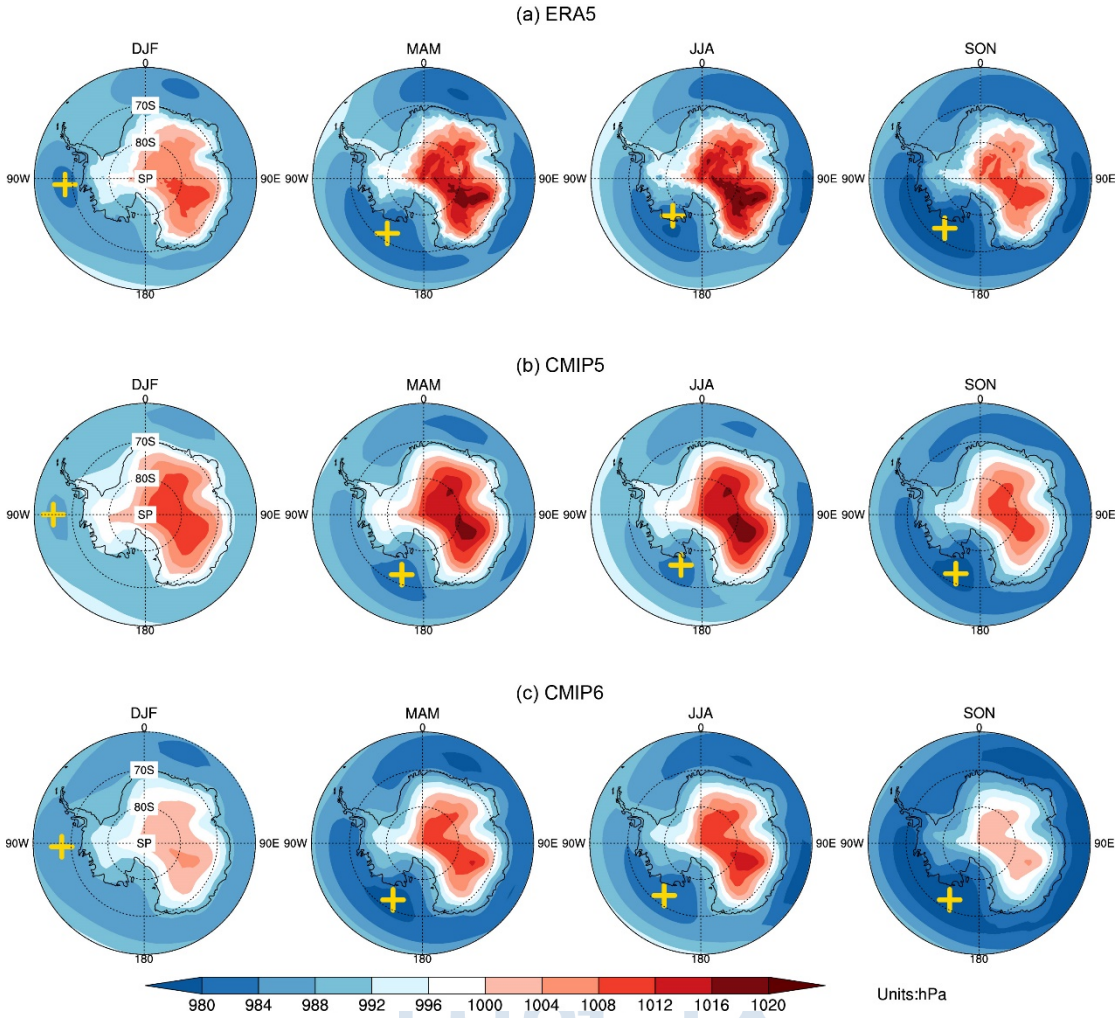

Figure 22. (a) Mean sea level pressure (hPa) averaged in boreal DJF, MAM, JJA and SON during 1979–2005 in (a) ERA5 reanalysis, (b) CMIP5 MME and (c) CMIP6 MME, respectively. The yellow crosses denote the centers of ASL.

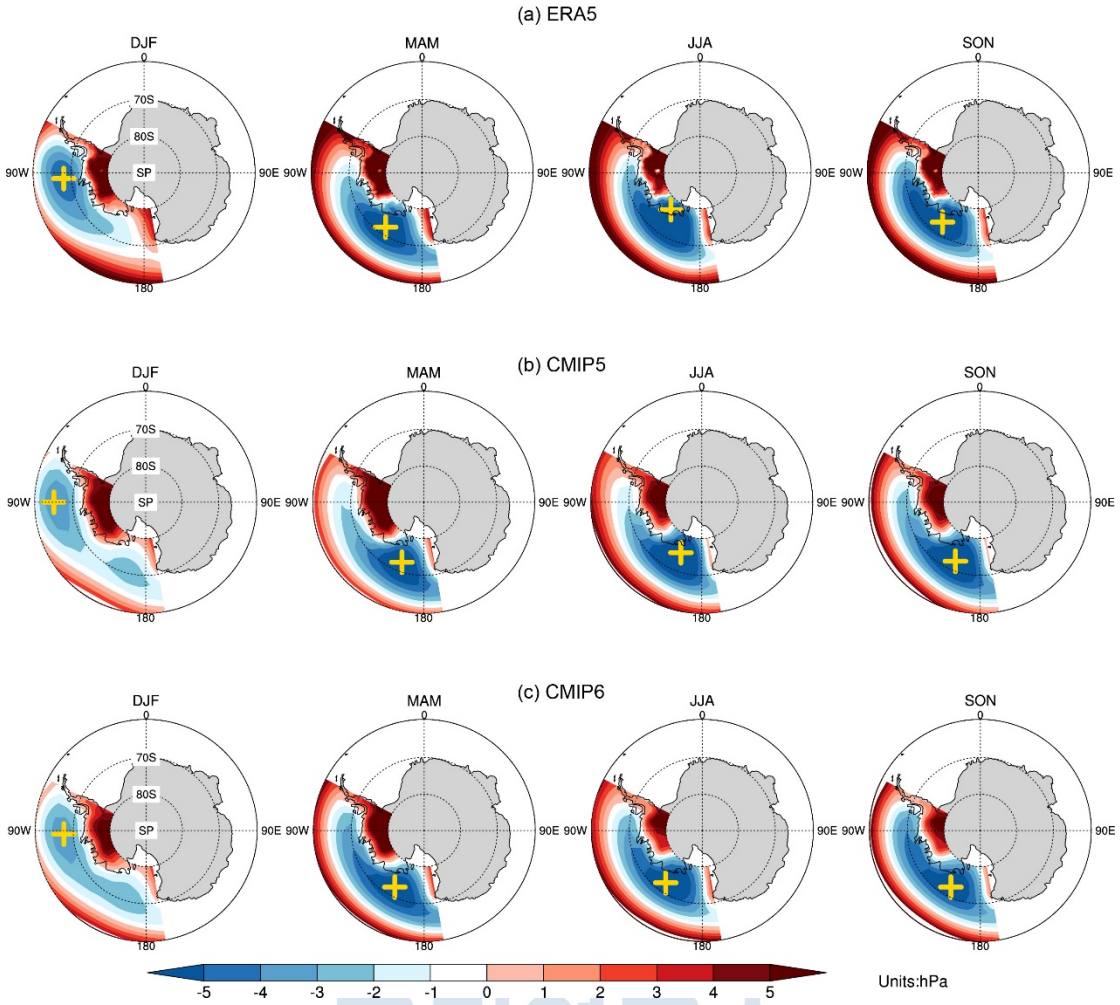

Figure 23. (a) Mean sea level pressure (hPa) anomalies obtained by subtracting the background area-averaged mean sea level pressure (area averaged over the region 60-80°S, 170-298°E) in boreal DJF, MAM, JJA and SON during 1979–2005 in (a) ERA5 reanalysis, (b) CMIP5 MME and (c) CMIP6 MME, respectively. The yellow crosses denote the centers of ASL.

In observation, distinct behaviors were identified using two types of ASL indices (actual central pressure and relative central pressure). The absolute depth of ASL reaches its minimum and maximum in austral summer and the following spring, which is well reproduced in most of the models and CMIP MME (Figure 24). In contract, the relative depth reaches its minimum and maximum in austral summer and winter, respectively (Figure 25). Although CMIP MME capture this characteristic, only some of CMIP models have good performance in simulating the seasonal variation of the ASL strength.

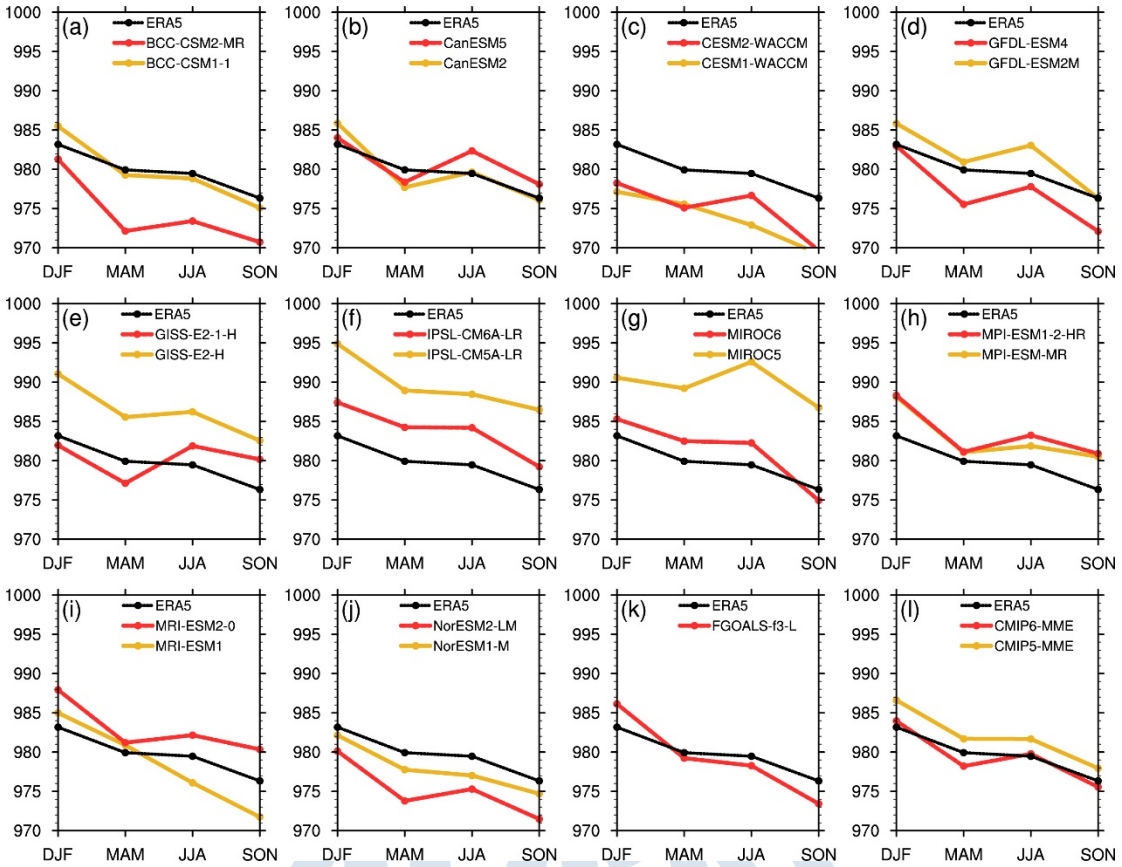

Figure 24. Time evolution of the absolute ASL strength in ERA5 reanalysis (black), (a) BCC-CSM1-1 and BCC-CMS2-MR, (b) CanESM2 and CanESM5, (c) CESM1-WACCM and CESM2-WACCM, (d) GFDL-ESM2M and GFDL-ESM4, (e) GISS-E2-H and GISS-E2-1-H, (f) IPSL-CM5A-LR and IPSL-CM6A-LR, (g) MIROC5 and MIROC6, (h) MPI-ESM-MR and MPI-ESM1-2-HR, (i) MRI-ESM1 and MRI-ESM2-0, (j) NorESM1-M and NorESM2-LM, (k) FOGALS-f3-L and (l) MME of CMIP5 models and CMIP6 models during 1979-2005, respectively. The results obtained from CMIP5 models and their CMIP6 versions are shown as yellow and red lines, respectively.

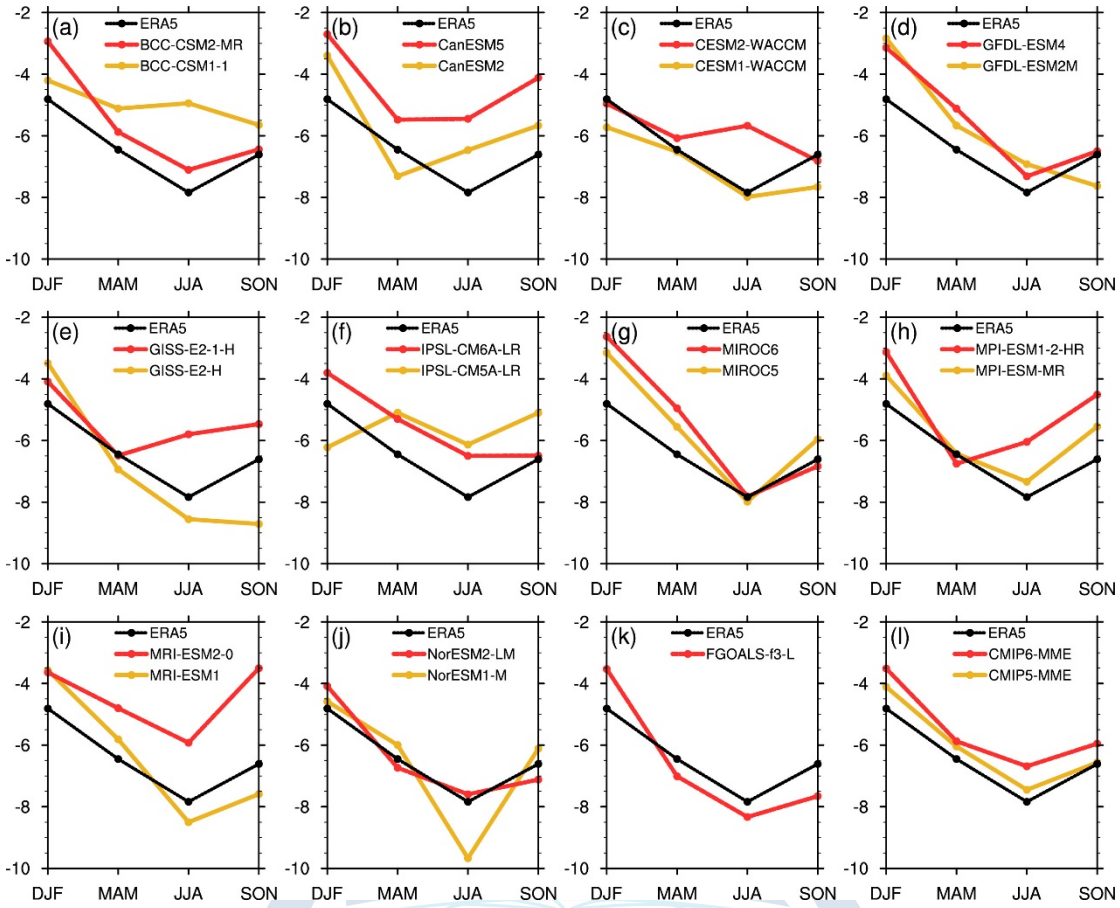

Figure 25. Same as Figure 24, but for relative central pressure.

Then the ASL location were comprehensively investigated (Figure 26 and Figure 27). Based on ERA5, the ASL center moves southward from austral summer to autumn gradually, reaches it southernmost position in winter and then moves northward in spring. Meanwhile, ASL locates around 35° W during austral autumn to the following spring and shifts to 90° W in winter. However, although the seasonal variation of the location of ASL center are simulated by CMIP5 and CMIP6 MME, half of the models fail to reproduce the characteristics.

In general, both of CMIP5 and CMIP6 MME could capture the spatial distribution and seasonal variation of the strength and location ASL. Compared with CMIP5, CMIP6 improve the performance of simulating ASL in most of the aspects. Among all the CMIP6 models evaluated in this study, CAS FGOALS-f2 has the best simulation skill. The results indicate the great potential of CMIP6 models in the study of ASL and its impact on Antarctic climate.

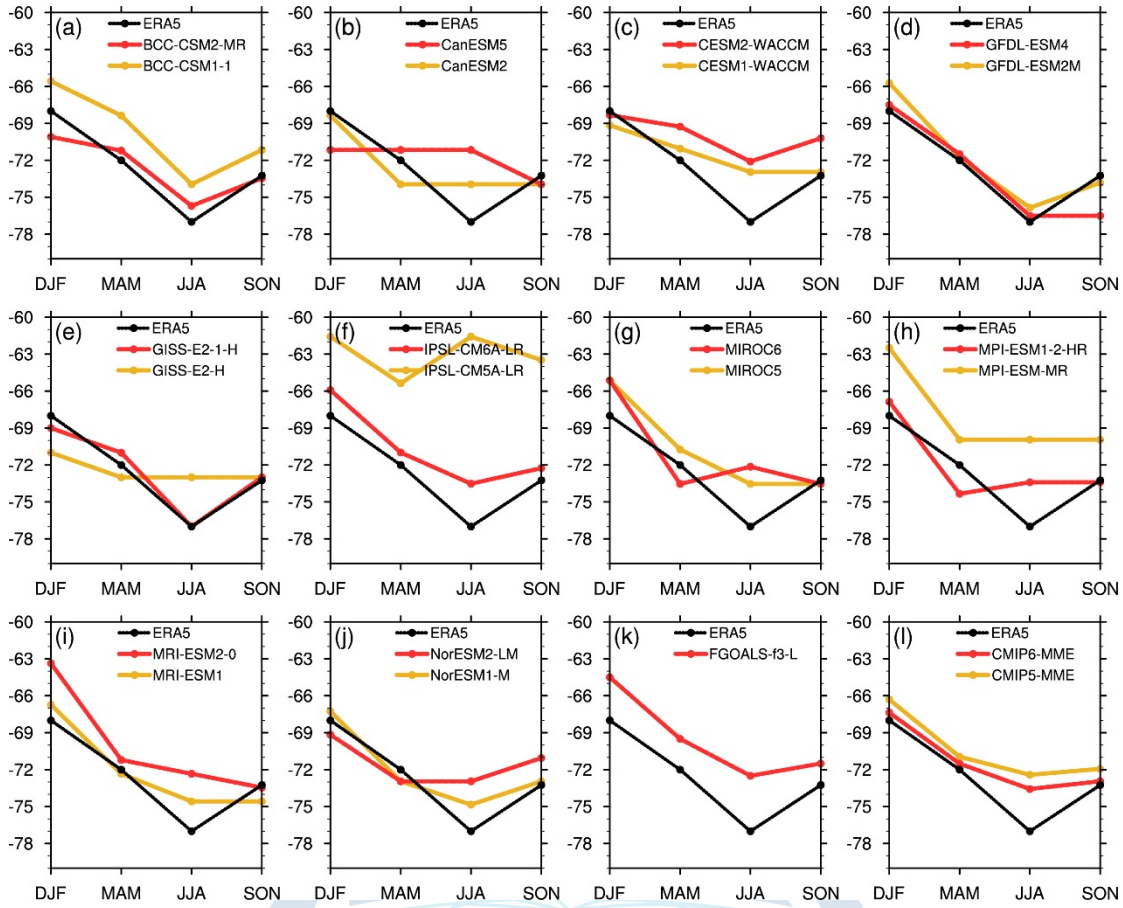

Figure 26. Same as Figure 24, but for the latitude of ASL center.

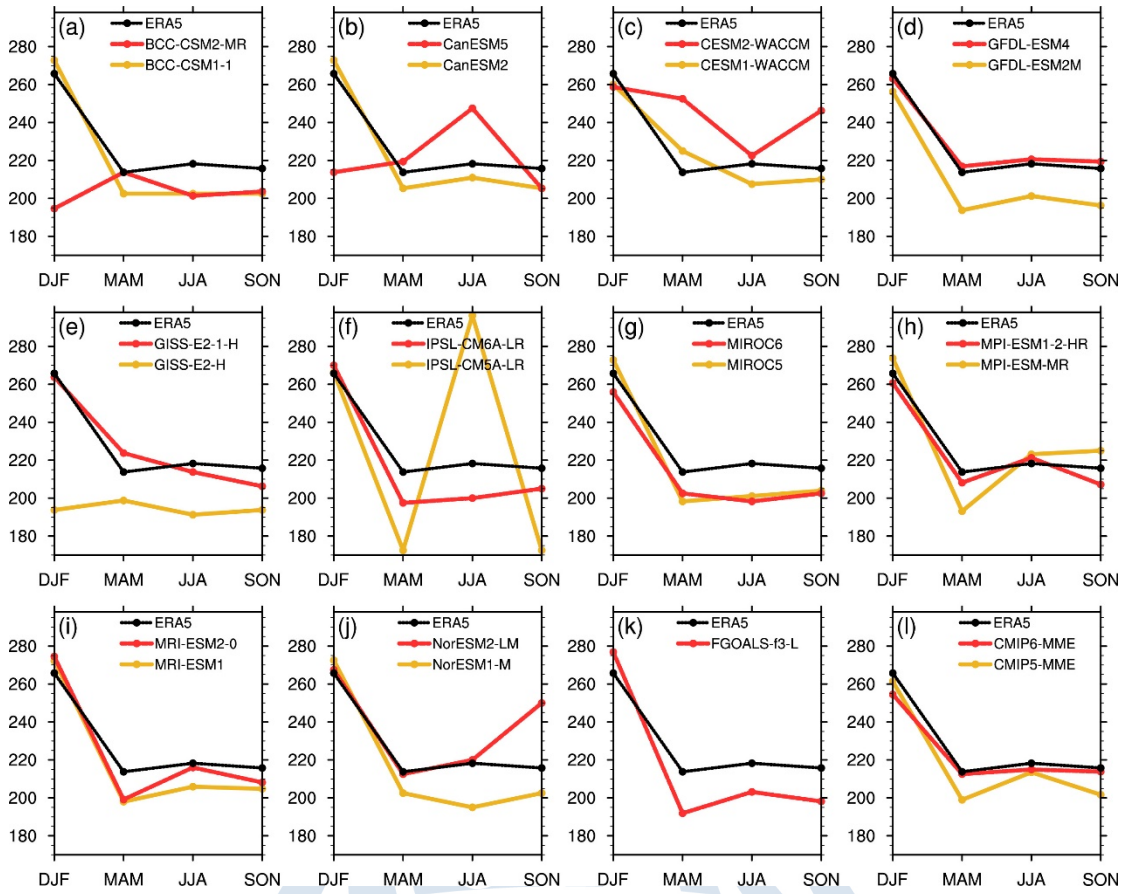

Figure 27. Same as Figure 24, but for the longitude of ASL center.

7) Simulated AAO in FGOALS-f2 model

In observation, AAO accounts for 49.5 % ,42.7%, 51.8%, 48.2% of the total variance, respectively, in summer, autumn, winter and spring. Compared with observation, the first dominant EOF mode (AAO) explains respectively 42.7%,37.3%, 33.2%, 37.7% of IAV variance in FGOALS-f2. The simulated percentage variance of AAO is very close to the observed, particularly in summertime. AAO is also called Southern Annular Mode (SAM) and its primary spatial feature of AAO is three major centers of positive SLP anomalies along mid-latitudes and one negative SLP anomalous center over polar region in observation during four seasons (Figure 28). The above major annular features are generally well captured in four seasons by FGOALS-f2. The major anomalous centers along South Pacific Ocean and polar region are almost consistent between observation and models. However, the Indian Ocean center is underestimated in summer and autumn seasons and South Antarctic Ocean center is overestimated in autumn and winter.

We further applied the Taylor diagram to evaluate the similarity of AAO spatial distribution simulated by FGOALS-f2 to its observed counterpart. Shown as in Figure 29, the spatial correlation coefficients (SCC), which are more than 0.7, evidently reached above 99% significance level in spring, summer and autumn. And spring and summer have a higher pattern correlation with observation. From the standard deviation (RMSD), the autumn and summer have variation that are lower than observed while the spring and winter have larger variation than observation. Compared with winter and summer, the spring and autumn have more realistic variation amplitude in AAO simulation.

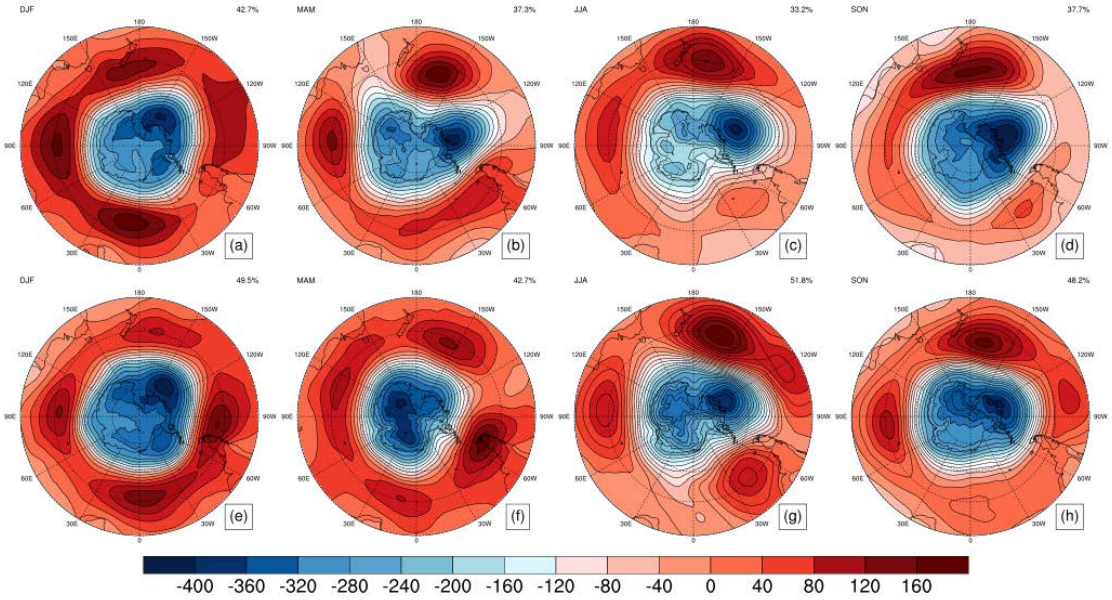

Figure 28. Spatial patterns of AAO in ERA-Interim for (a)DJF, (b)MAM, (c)JJA, and (d)SON for the period of 1979-2005. (e)-(f) as in (a)-(d) but showing the results in FGOALS-f2.

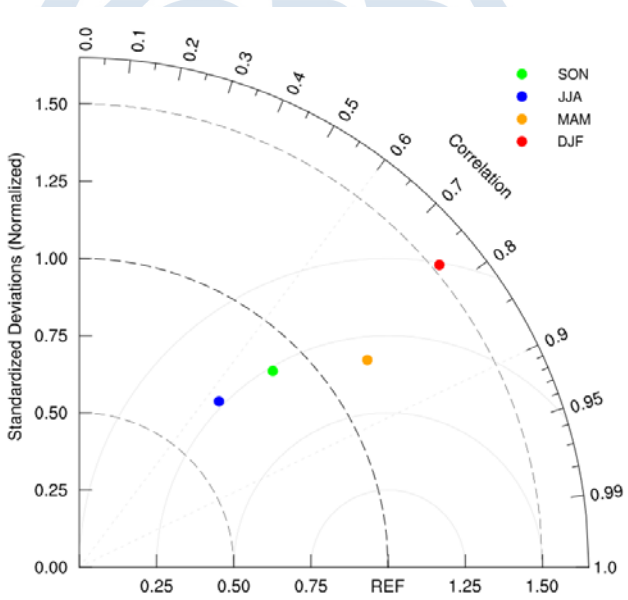

Figure 29. The Taylor diagram of the spatial patterns of AAO in four seasons during 1979-2005. The red point stand for DJF, orange point for MAM, blue point for JJA and green point for SON. The radial distance of each point from the origin is in direct proportional to the standard deviation of the modelled AAO pattern of FGOALS-f2 relative to the observed AAO pattern of the ERA-Interim. The correlation coefficient between patterns in observation and in model is given by the azimuthal position of the point, and their RMS difference is expressed by the distance of each point from the reference point(REF). Additionally, Y axis presents ratio of SD.

We also examined the interannual variability and trend of AAO index from original time series in both ERA-Interim and FGOALS-f2 (Figure 30). Previous study focused most on AAO trend and variability on

summer considering the trend and the impact of ENSO are most notable during DJF period(m_aao1,2), and here we exhibit IAV of AAO for the four seasons. A robust interannual change can be identified in each season, and particularly in ERA-Interim the evident interannual change during summer is characterized by a transition from a negative phase to a positive one approximately in 1982. This character is also seen in FGOALS-f2 during autumn. Besides, in summer, AAO shows a positive trend of 0.44 per decade and is statistically significant at 0.1 level, which has also been reported in previous studies (Arblaster and Meehl, 2006; aao3). FGOALS-f2 has the ability to capture the increasing trend in summer and autumn although the trend is underestimated and not as significant as observed. In contrast to ERA-Interim, FGOALS-f2 performs the insignificant (at 90% confidence level) increase trend of 0.45 per decade in winter.

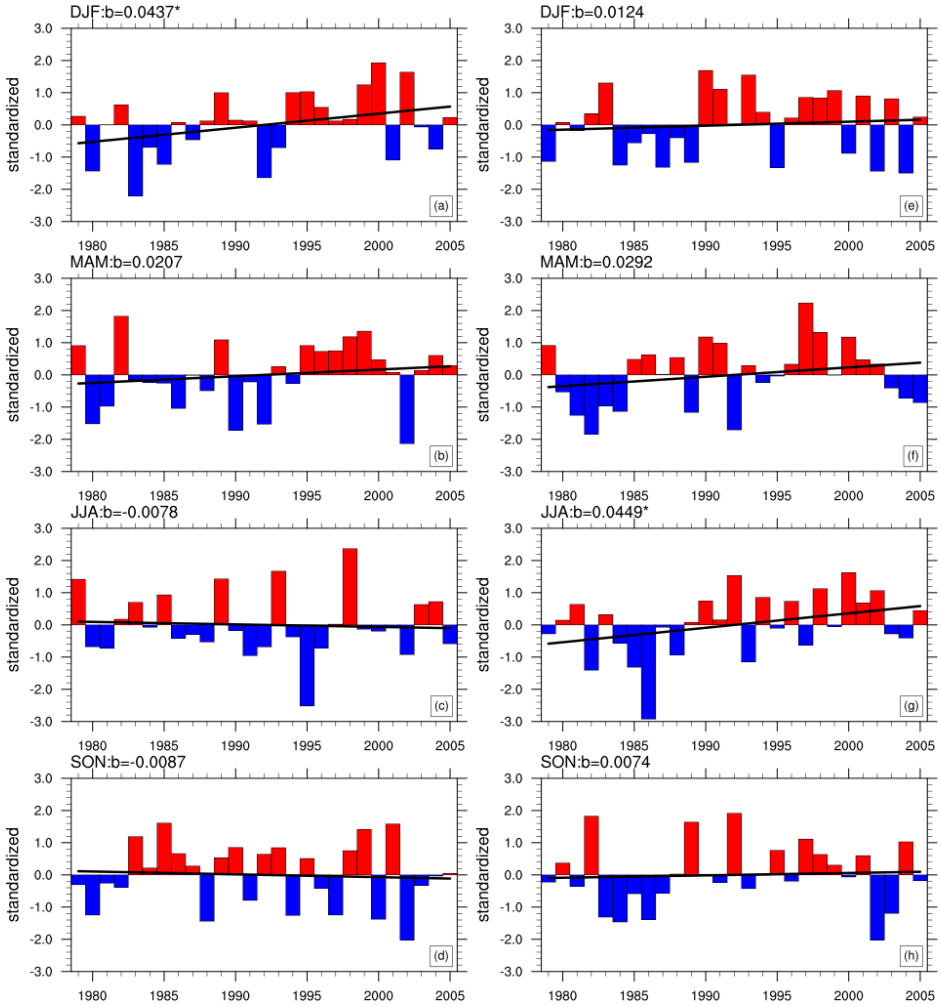

Figure 30. The AAO index in ERA-Interim for (a) DJF (b) MAM, (c) JJA, and (d) SON for the period of 1979-2005. (e)-(f) as in (a)-(d) but showing the results of FGOALS-f2 model data. The black lines present fitted lines between AAO index and time series, and b indicates the linear trends.

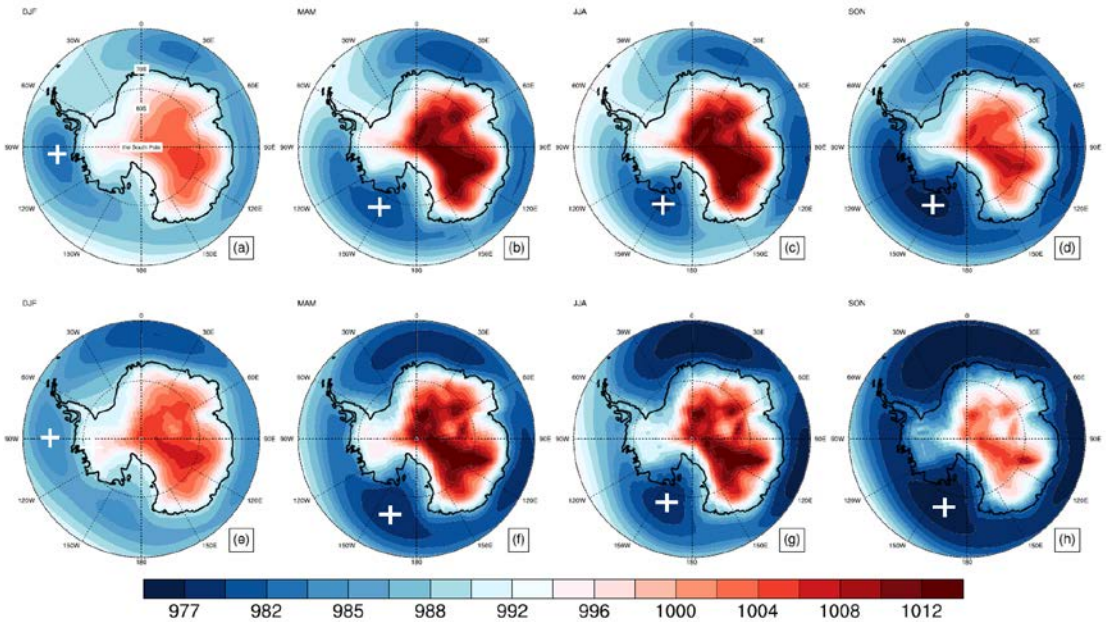

Figure 31. Seasonal MSLP(hPa) averaged 27-yr period of 1979-2005 in (a)-(d) ERA-Interim and (e)-(h) FGOALS-f2 for DJF, MAM, JJA, SON respectively. The white cross marks the center of the ASL.

8) Simulated Amundsen Sea Low in FGOALS-f2 model

The Amundsen Sea Low (ASL) is a climatological area of low pressure located in the South of the West Antarctica defined broadly as 170°—298° E, 80°—60° S. It can be recognized as a significant component of AAO which also has direct influence on Antarctic climate. Seasonal mean state of ASL is shown in Figure 32, three large negative pressure regions are basically observed in four seasons around Antarctica, which is also caught by FGOALS-f2. ASL is over the Pacific sector of the Southern Ocean and has the largest intensity compared with other two low systems, which coincides with modeled spatial pattern except in summer. During summer, the center of the ASL has remarkable westward migration, extending from Antarctic Peninsula to the Bellingshausen Sea with reaching its maximum amplitude in Amundsen Sea region. The Absolute pressure in ASL region reach its minimum in austral autumn and maximum in austral winter. Intuitively, FGOALS-f2 is able to capture the westward migration in austral summer and the seasonal variation of its intensity.

To exam the seasonal variation of ASL longitude and strength, we plot the 27-yr seasonal ASL indices and their mean for four seasons in ERA-Interim and FGOALS-f2. ASL is observed to migrate westward from 260° E to 215° E between summer and winter, and also deepens from summer to winter, with its minimum relative central pressure of -9.1hPa occurring in winter and its maximum of -6.4hPa in summer. In FGOALS-f2, simulated ASL has a 30° westward shift during summer and autumn, and reaches its minimum of -8.7 hPa in winter, as well as maximum of -6.1 hPa in summer. Corresponding pattern of ASL migration and deepening is well identified comparing to observation, although the model evidently underestimates ASL intensity in summer, winter and spring and overestimates it in autumn and additionally, present a more westward center in summer and autumn. As displayed in Figure 32, red (blue) lines of model data and the reanalysis data overlap in all seasons, which denotes that FGOALS-f2 have no significant difference with ERA-interim in presenting seasonal ASL longitude and relative central pressure. In terms of the correlation coefficients between these two quantities, no statistically significant relationship of ASL longitude and relative central pressure is found in observation, while this significant relationship is detected in the model during summer($r \approx -0.43$), autumn(($r \approx 0.40$) and spring(($r \approx 0.50$), indicating that during summer the ASL deepens the father westwards it located.

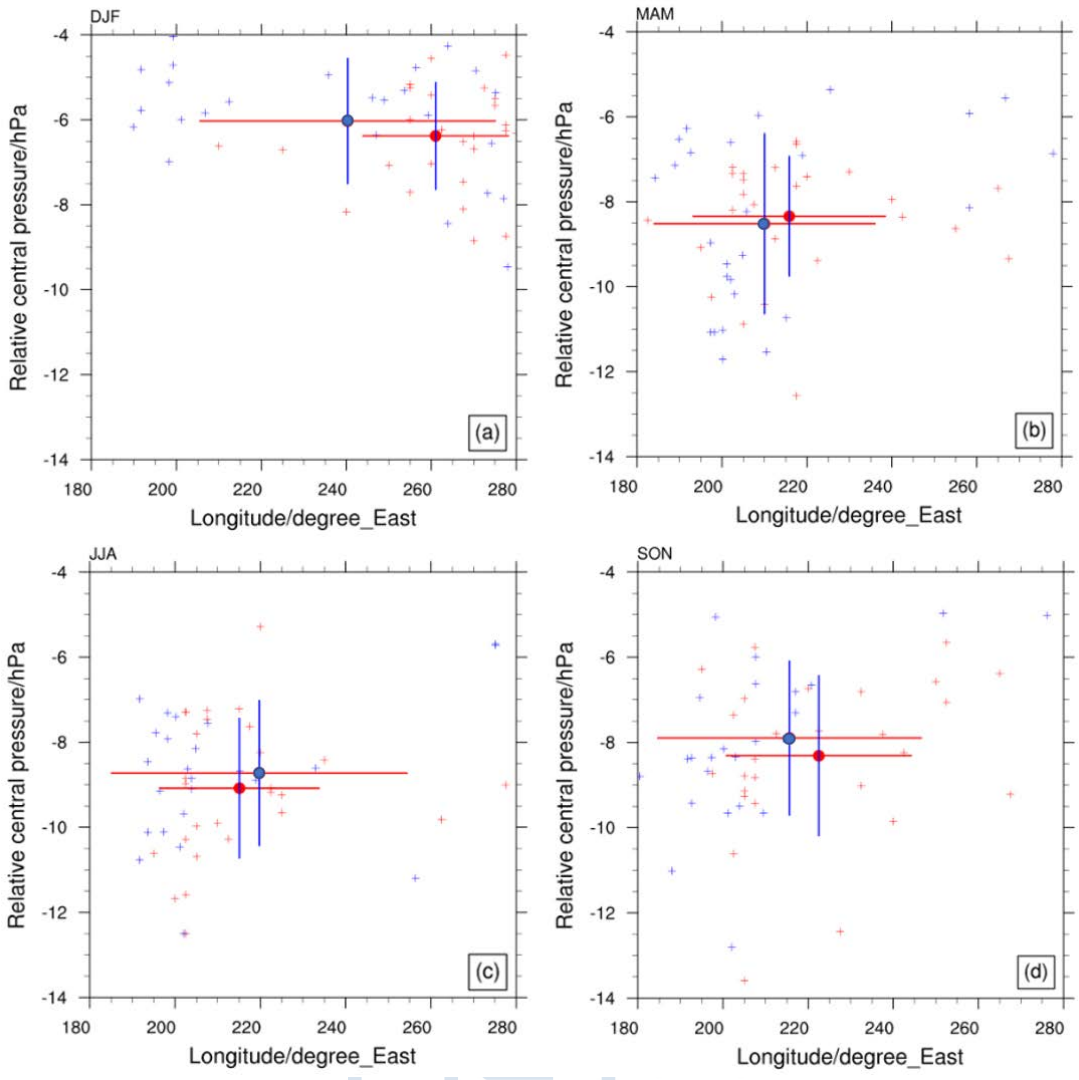

Figure 32. Scatter plot of the seasonal ASL longitudinal position(°E) and relative central pressure (hPa) for (a) DJF, (b) MAM, (c) JJA, and (d) SON for the period of 1979-2005. Red(blue) crosses represent seasonal ASL indices in observation(model), while Red(blue) circles express seasonal mean value. Solid red(blue) lines show the one standard deviation of relative central pressure(longitudes).

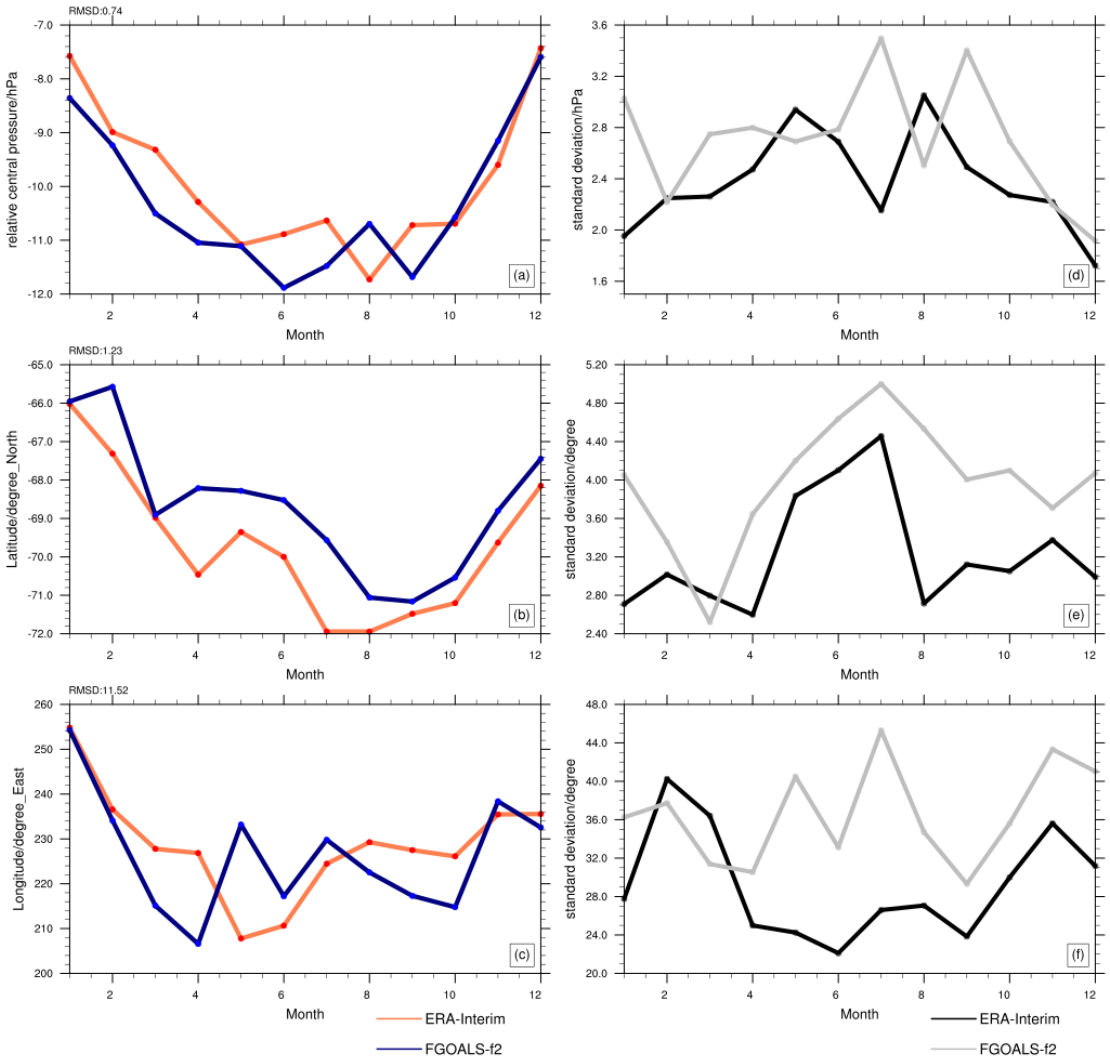

Figure 33. Intra-annual variation of ASL (a)relative central pressure (hPa), (b) latitude (°N) and (c)longitude (°E) in ERA-Interim and FGOALS-f2 for the period from 1979 to 2010. (d)-(f) are same as in (a)-(c) but for interannual one standard error. The annual rms deviation (RMSD) for FGOALS-f2 relative to ERA-Interim is shown in the top-left corner of panel (a), (b)and (c) respectively.

Intra-annual change of ASL location and intensity spanning 1979-2005 is also examined. The interannual standard deviation of model outputs is greater than the reanalysis in most months, which implies that model results have more uncertainty and larger divergence. Shown in Figure 34(a), a deepest pressure of -11.7 hPa occurs in August (summer) and shallowest of -7.4 hPa occurs in December (winter). The relative central pressure decreases in two periods: from January to March and from July to August, which briefly conforms with the result by Tuner () suggesting that the twice-yearly cycle of MSLP in the Antarctic circumpolar trough involved the semiannual oscillation (SAO). The greatest amplitude of the SAO appears in the Amundsen Seas, so the twice-yearly cycle of SLP minima can be clearly caught in observation. As

seen in the plot, FGOALS-f2 precisely predicts the deepening period from January to March and months when extremum of ASL pressure occurs, although model underestimates ASL depth in most months and overestimates it in August, October and November. Besides, it also characterizes twice-yearly shift associated with semiannual oscillation mentioned above.

ASL longitudinal location has its farthest west in March in Ross Sea (208°E) and farthest east in Amundsen Sea (255°E) in January. It is observed annual cycle featured as westward migration during January to March and eastward migration during March to December, combined with characteristics of shifts of latitude location (Figure 34b) that the ASL center is prone to be farthest south during the summer months, and farther north during the winter months, reflecting the spatial variability pattern displayed in Figure 3. The model shows misrepresentation of regular annual pattern of longitude movement, as it displays four westward migration in a year. What's more, the southern (northern) shift in winter (summer) months for latitudinal position of the ASL is reproduced roughly, although modeled ASL latitude shows a southern bias in all months.

We further examine the intra-annual variation of ASL longitude and relative central pressure in the 15 CMIP5 climate models to reveal whether FGOALS-f2 has better performance than CMIP5 models. Previous study has examined the Amundsen-Bellingshausen Sea Low(ABSL) annual cycle in 17 CMIP5 climate models run with historical forcing (M_asl), and found that no one model has the ability to simulate both the intra-annual change of relative central pressure and longitude reasonably accurately, making it difficult to assess their skill in representing the ASL. Consequently, we plot respective RMSD value against each other in Figure 35. FGOALS-f2 ranks fifth at simulating longitude(RSMD of 11.52°) and ranks fourth for relative central pressure(RMSD of 0.74hPa) in 15 models, which denotes FGOALS-f2 has better performance than most CMIP5 models in reproduce intra-annual variation of ASL. Among 14 CMIP5 models, the CCSM4 model ranks first at simulating both relative central pressure and longitude, with lowest RMSD of 0.57hPa and RMSD of 8.32° respectively. CCSM4 largely captures both the deepening of the ASL over January to April and its weakening over August to December, and simulates more authentic value of ASL intensity than FGOALS-f2, which explains the lowest relative central pressure RMSD. CCSM4 broadly simulates both the westward migration of the ASL from summer to winter, but still has bias in most months as FGOALS-f2. Basically, with the exception of the two outliers (MRI-CGCM3and INM-CM4), that biases in longitude and relative central pressure tend to increase together.

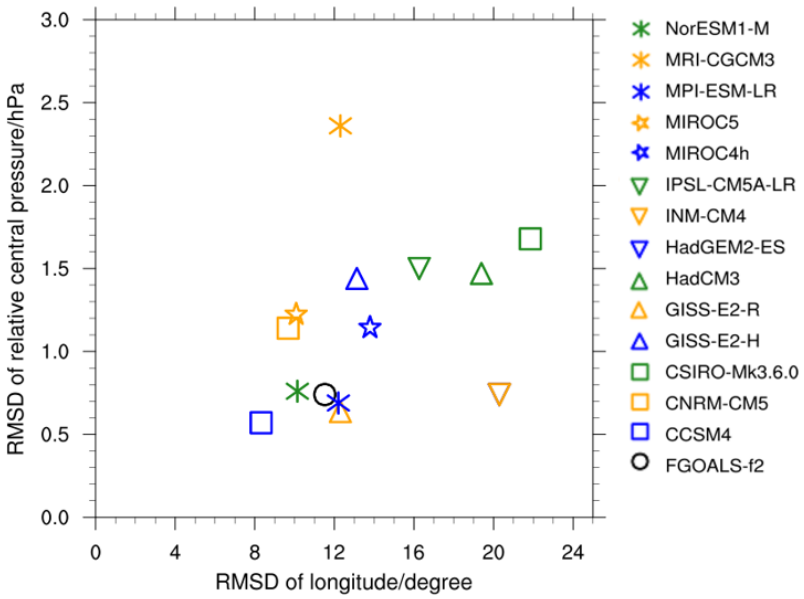

Figure 34. Scatterplot of the annual RMSD for FGOALS-f2 and 14 CMIP5 model relative to ERA-Interim of ASL relative central pressure (hPa) and longitude (°) for the period 1979–2005.

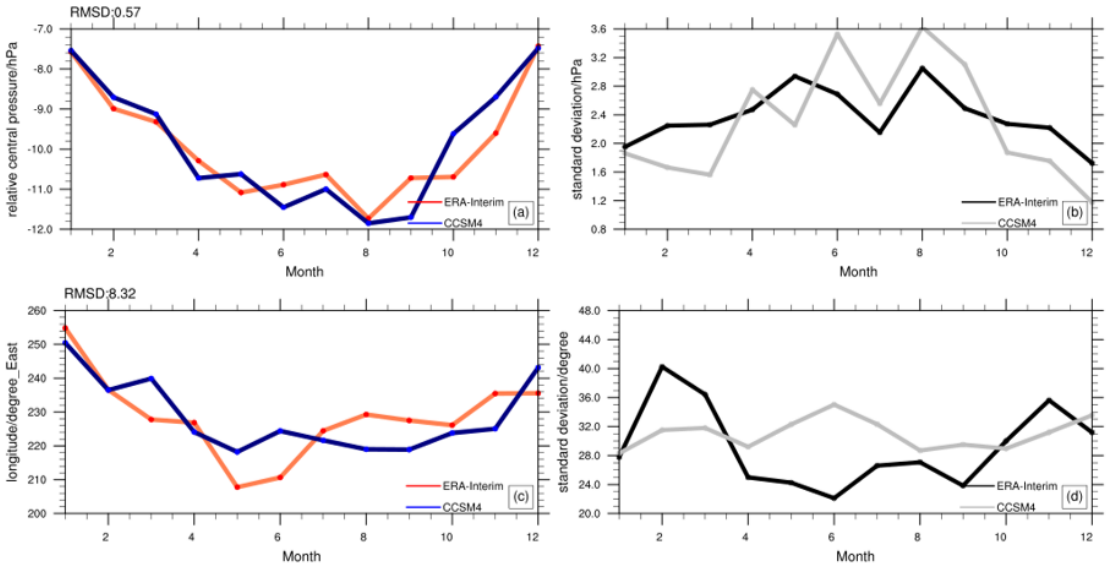

Figure 35. Intra-annual variation of ASL (a)relative central pressure (hPa), (c) longitude (°E) in ERA-Interim and CCSM4 for the period from 1979 to 2010. (b)&(d) are same as in (a)&(c) but for interannual one standard error.

9) Interannual influence of Antarctic Oscillation on haze pollution in North China during the last four decades

We first examined the spatial distribution of raw (unfiltered) and high-frequency (<10yr) correlation coefficients between the 3-months moving AAO indices from March-April-May (MAM, ten months in advance) to December-January-February (DJF, in simultaneous) and the boreal winter mean visibilities at 542 synoptic meteorological stations around China. Intuitively, the August-September-October (ASO) AAO was most significant correlated with the winter visibility in North China (NC) (Figure 36, the other Maps omitted). To quantitatively evaluate the correlations in different lead-lag times and different areas, the correlation coefficients between the boreal winter mean visibilities in East China (EC, east of 105 ºE), North China (NC, east of 105ºE and between 30 and 43ºN) and South China (SC, east of 105ºE and south of 30 ºN) and the AAO indices in different lead times were calculated (Table 3). In the raw correlations (r1), the maximum correlations occurred between ASO-AAO and DJF visibility in both EC (0.44) and NC (0.50), respectively. Both of them are significant at 95% level. Furthermore, most of the high-frequency correlations are larger than the raw correlations. This suggests that the links between the winter visibility changes in eastern China and ASO-AAO activities are very stable from year to year, especially in NC. The temporal variability of the mean winter visibilities in EC and NC are generally consistent with the annual ASO-AAO index (Figure 36b). For example, the NC visibility minimized in winter 2013/14, which was corresponding to a minimum AAO in ASO 2013. The significantly positive correlations suggest that the enhanced AAO in ASO season is conducive to the increase of visibility (namely the improvement of air quality, or the reduction of air pollutions) in NC in winter, and vice versa.

How does the variability of AAO affect the winter air pollution in North China? As mentioned in Introduction, the haze pollutions in Beijing or even eastern China are close related to anomalous local and large-scale meteorological conditions. Thus a test of the possible response of the surface winds to ASO-AAO were performed. Based on the surface winds records at the synoptic meteorological stations and linear regression analysis, the anomalies surface winds in boreal winter corresponding to one unit of AAO index in ASO season were investigated. It should be noted that, in order to reduce the possible effects of low-frequency variation or long-term trends and to examine whether or not the response on an interannual timescale is stable, all time series were high-pass filtered before regression analyses. As shown in Figure

37a, the anomalous northwesterly dominated in NC areas, which suggested that the enhanced ASO-AAO causes a stronger northwest winds in NC areas than the climatological surface winds (Figure 37b). The stronger northwest winds are very conducive to the spread and elimination of air pollutants, and then the reduction of pollutant concentrations will certainly promote the improvement of visibility (Zhang et al., 2016, 2017).

Furthermore, we wonder whether there exist large scale anomalous circulations that matched the local anomalous northwest winds. Thus the responses of the regional atmospheric circulations to ASO-AAO were also examined, such as sea level pressure (SLP), zonal and meridional winds at 850 hPa (U&V850), geopotential height field at 500 hPa (H500), zonal and meridional winds at 200 hPa (U&V200) (Figure 38). In SLP, the pressure increased in most of Asian continent and decreased in Northeast China to northwest Pacific (Figure 38). This pattern suggests that the pressure gradient over east Asian increase as the enhanced ASO-AAO. In U&V850, an anomalous cyclonic circulation occurred in the areas form northern China to northwest Pacific, and the anomalous northerly winds dominated northern China (Figure 38b). This suggests that an anomalous northerly advection from high latitude to northern China as the increasing of ASO-AAO. In H500, the geopotential height decreased from northern China through Korean peninsula to Japan, which implies a deepening of East Asian trough (Figure 38c). In U&V200, the anomalous cyclonic circulation dominated the northern China, which implies the south (north) of the East Asian jet stream strengthened (weakened), coinciding with the anomalous ascending (sinking) motions that occurred in the south (north) of the jet stream entrance at the upper troposphere, which will lead to a strengthening northerly that appeared in the lower troposphere (Figure 38). In generally, all of the response patterns from the lower to upper troposphere suggest that the enhanced ASO-AAO can cause a stronger East Asian winter monsoon. The strengthened northerly wind lead to the reduction of air pollution and improvement of visibility in eastern China, especially in North China.

The correlation or regression analyses after high-pass filtering can effectively eliminate the influence of global warming and other inter-decadal changes or long-term trends on the links between air pollution in NC and AAO activity. However, the interannual climates in both southern and northern hemispheres are largely impacted by El Niño/Southern Oscillation (ENSO), especially in low latitudes (Wang et al., 2000). Thus there may still be unreal relationships between ASO-AAO and air pollutions in boreal winter in NC due to the simultaneous modulation by the ENSO. In order to examine whether or not the correspondences

between ASO-AAO and DJF-VIS in China are stable and independent from ENSO, we removed ENSO signals in the variables of interest by means of regression analysis. We simply fit the ASO Niño3.4 SST to ASO-AAO and DJF-VIS variables by using the least-square technique. Then the estimated ENSO-related components were subtracted from the original time series, and the residuals were regarded as ENSO-free parts (i.e., ASO-AAO-ENSO-free, DJF-VIS-ENSO-free) and subjected to the analysis.

The spatial distribution of high-frequency correlation coefficients between the ASO-AAO-ENSO-free and DJF-VIS-ENSO-free in China were examined. Intuitively, there are very few differences between Figure 36a (correlations between ASO-AAO and DJF-VIS with ENSO) and Figure 39a (correlations between ASO-AAO and DJF-VIS without ENSO). The spatial correlation coefficient between them is 0.996, with significant at 99% level. After ENSO-removed, the high-frequency (original) correlation coefficients between the average visibility in boreal winter in EC, NC, SC and ASO-AAO are 0.53 (0.57), 0.56 (0.60) and 0.27 (0.26), respectively. All of them are significant at 99% level. Unexpectedly, there are a certain improvement of the correlations between the series of ASO-AAO-ENSO-free and DJF-VIS-ENSO-free in NC and EC. Moreover, the ENSO-removed surface winds (Figure 39b), SLP, UV850, H500 and UV200 (Figures omitted) in boreal winter corresponding to ASO-AAO-ENSO-free are generally same as the original relationships (Figure 36). This phenomena indicated that the activity of ASO-AAO exert an important role on the winter air pollution in NC without distinct interference from ENSO.

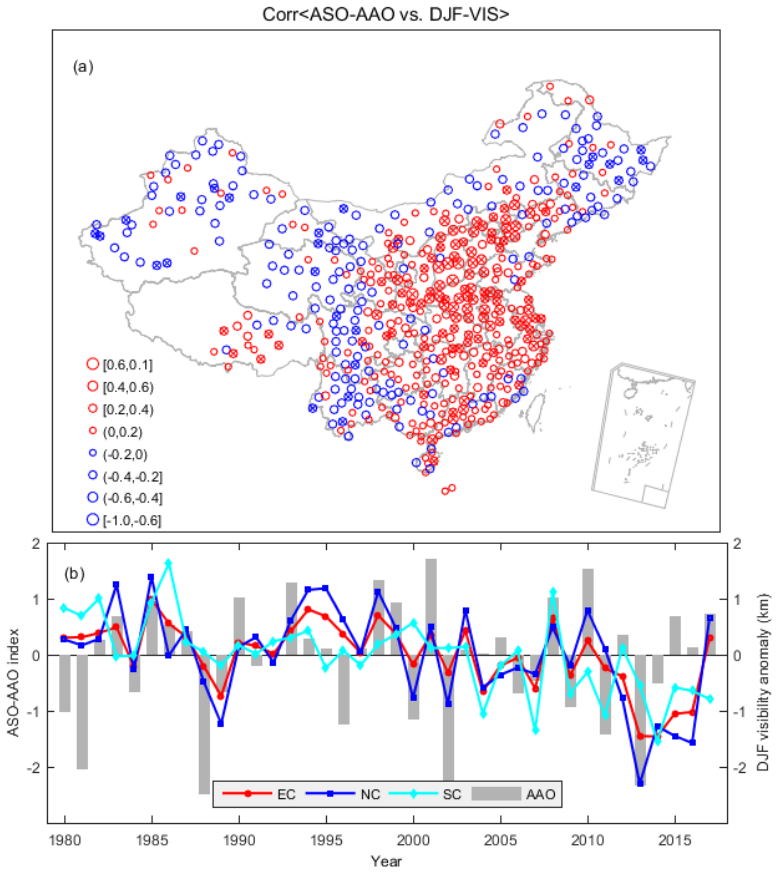

Figure 36. The spatial distribution of high-frequency (<10yr) correlation coefficients between the AAO index in ASO (ASO-AAO) and the mean visibility in boreal winter (DJF-VIS) in China (a) and the original curves of DJF visibility anomaly of EC, NC, and SC and ASO-AAO index (b)

Table 3. Correlation coefficients between leading AAO index and DJF visibility in East China (EC), North China (NC) and South China (SC)

		MAM	AMJ	MJJ	JJA	JAS	ASO	SON	OND	NDJ	DJF
EC	*r*1	-0.17	-0.19	-0.19	0.01	0.24	0.44**	0.34**	0.29*	0.20	-0.01
	*r*2	-0.07	-0.02	0.02	0.26*	0.41**	0.50**	0.40**	0.37**	0.17	0.00
NC	*r*1	-0.08	-0.12	-0.13	0.05	0.26*	0.50**	0.39**	0.39**	0.30*	0.10
	*r*2	0.01	0.05	0.07	0.28*	0.39**	0.52**	0.42**	0.48**	0.28*	0.12
SC	*r*1	-0.29*	-0.26*	-0.20	0.01	0.12	0.17	0.14	0.00	-0.12	-0.29*
	*r*2	-0.12	-0.08	0.01	0.19	0.29*	0.27*	0.21	-0.01	-0.09	-0.19

** denote significant at 95% level and * denote significant at 90% level. The *r*1 and *r*2 terms indicate the raw correlation and high-frequency (<10 years) correlation, respectively. MAM denotes the mean of March, April and May, AMJ denotes the mean of April, May and June, and so on.

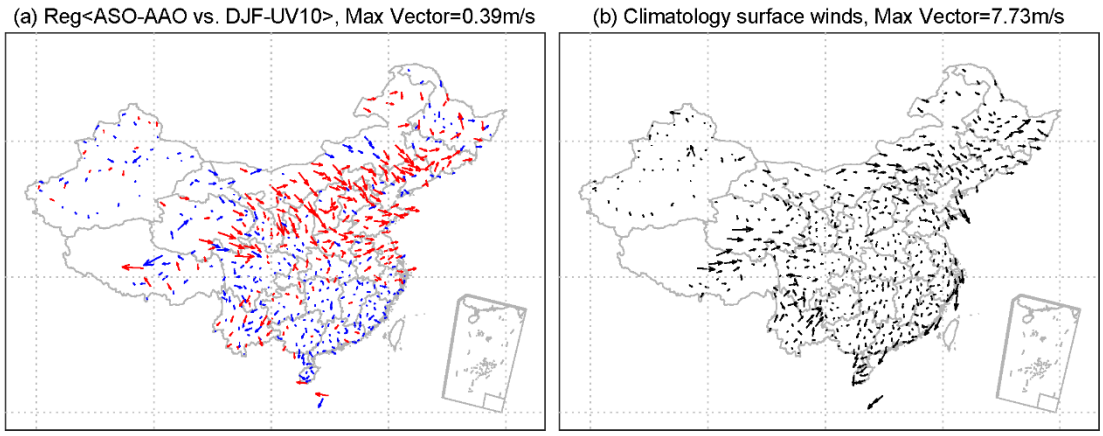

Figure 37. The anomalies surface winds in boreal winter (DJF-UV10) corresponding to one unit of the AAO index in ASO (ASO-AAO) (a) and the climatological mean surface winds in boreal winter (b) (The red vectors in Figure 37a denote significance at 95% level)

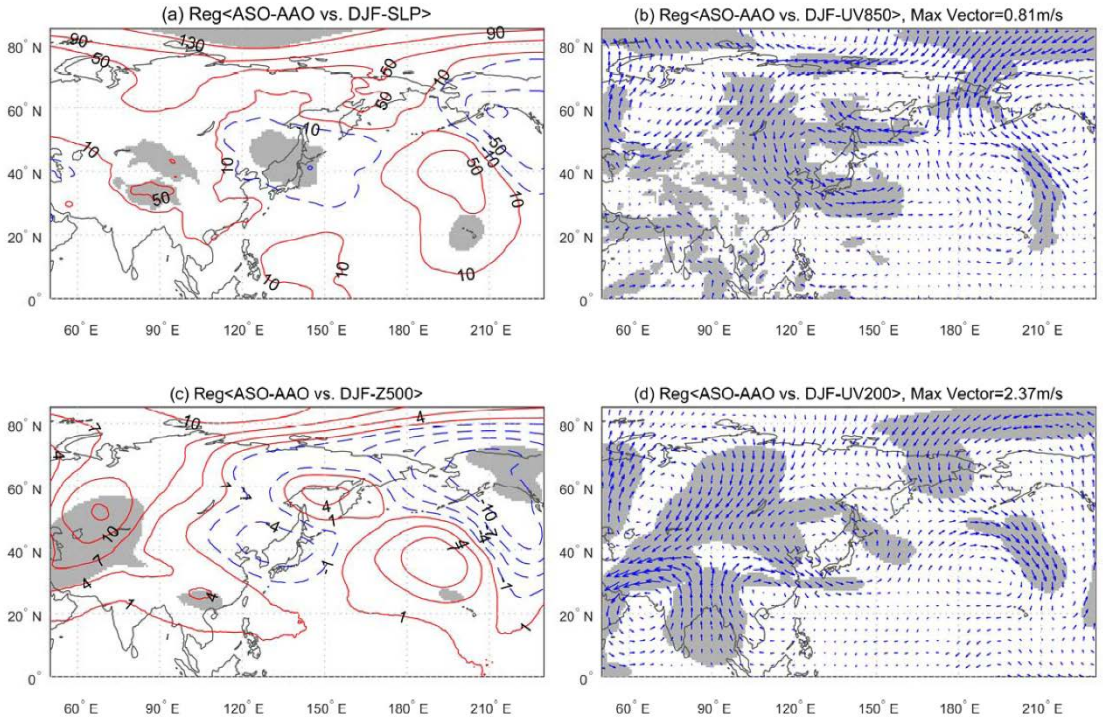

Figure 38. The anomalies SLP (a), horizontal winds at 850 hPa (b), geopotential height at 500 hPa (c) and horizontal winds at 200 hPa (d) corresponding to one unit of AAO index in ASO (ASO-AAO) (significant at 90% level are indicated by gray shadings)

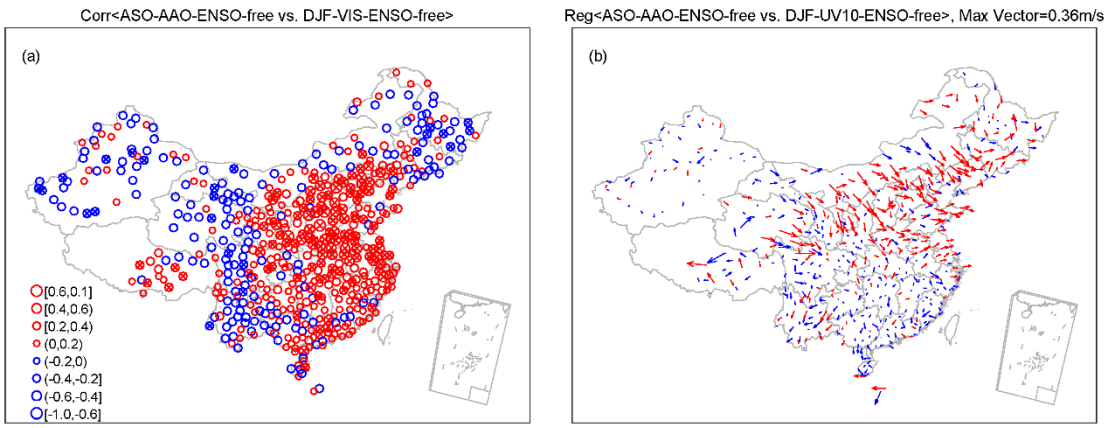

Figure 39. The spatial distribution of high-frequency (<10yr) correlation coefficients between the ASO-AAO-ENSO-free and DJF-VIS-ENSO-free in China (a) and the ENSO-removed surface winds in boreal winter (DJF-UV10-ENSO-free) corresponding to one unit of ASO-AAO-ENSO-free (b)

10) The EOF1 of SAT variability derived by observations

We firstly calculated variance explanation of detrended SAT to total variance of SAT in 1979-2004 and 2051-2099. In the READER data, 16 of 19 stations showed a high variance explanation (80%) along the coastline of the Antarctica and the AP in 1979-2004 (Figure 40a). The ERA-Interim Reanalysis dataset also showed a high variance explanation exceeding 90% in the Antarctica and most of southern oceans. Only the southern portion of Indian Ocean and the Ross Sea shows a weak ratio of 70-80% (Figure 40). Variance explanation of detrended SAT to total variance of SAT from the CMIP5 simulations was calculated in 1979-2004 and 2051-2099. For clarity, ensembles of variance explanations of the CMIP5 models were shown (Figure 40). Except that the southern portion of the Indian Ocean and the Ross Sea had a variance explanation of 80-90%, the ensemble of variance explanations in 1979-2004 was 90% in the Antarctica and its surrounding oceans. In contrast to 1979-2004, the ensemble of variance explanations in 2051-2099 decreases, with a variance explanation of 50-60% in the Antarctica, 60-70% in southern portions of the Pacific and the Atlantic Ocean, and 40-60% in southern portion of the Indian Ocean. In general, detrended SAT explains at least 50% of SAT variance in 1979-2004 and 2051-2099. Thus, we will analyze the EOF1 of detrended SAT variability in the Antarctica, i.e., the EOF1 of SAT variability at an interannual time scale in the Antarctica.

Figure 41a shows the EOF1 of SAT variability at an interannual time scale derived from the READER data in 1979-2004. Negative anomalies were dominant in the EOF1. Of all 19 stations, 13 stations showed negative anomalies from the South Pole to coastal regions, with magnitudes less than -0.3. Positive anomalies were sparse, mainly locating in the north of the AP with magnitudes of 0.2-0.3. The EOF1 explained 43% of detrended SAT variance in the Antarctica. The opposite anomalies between EA and AP imply a positive (negative) SAT anomaly in the EA with a negative (positive) SAT anomaly in the AP at an interannual time scale during 1979-2004. The ERA-Interim Reanalysis dataset reproduced the EOF1 of detrended SAT variability from the READER data, i.e., negative anomalies in the Antarctica with a center in the EA and positive ones in the AP and over the Bellingshausen Sea (Figure 41b). The variance explanation of the EOF1 derived by the ERA-Interim Reanalysis dataset was 42%. The similarity in the EOF1 derived by two datasets was supported by a high correlation of the first principal component of two datasets with a correlation coefficient of 0.91, significant at the 95% confidence level (Figure 41c). However, the EOF1 derived by the ERA-Interim Reanalysis dataset revealed more information than the READER data. The negative anomalies in the EA were triple or four times to positive ones in the AP, implying a larger variance

of SAT in the EA than in the AP at an interannual time scale. Moreover, positive anomalies in the Bellingshausen Sea in association with negative anomalies in the EA were indicated by the ERA-Interim Reanalysis dataset rather than the READER data.

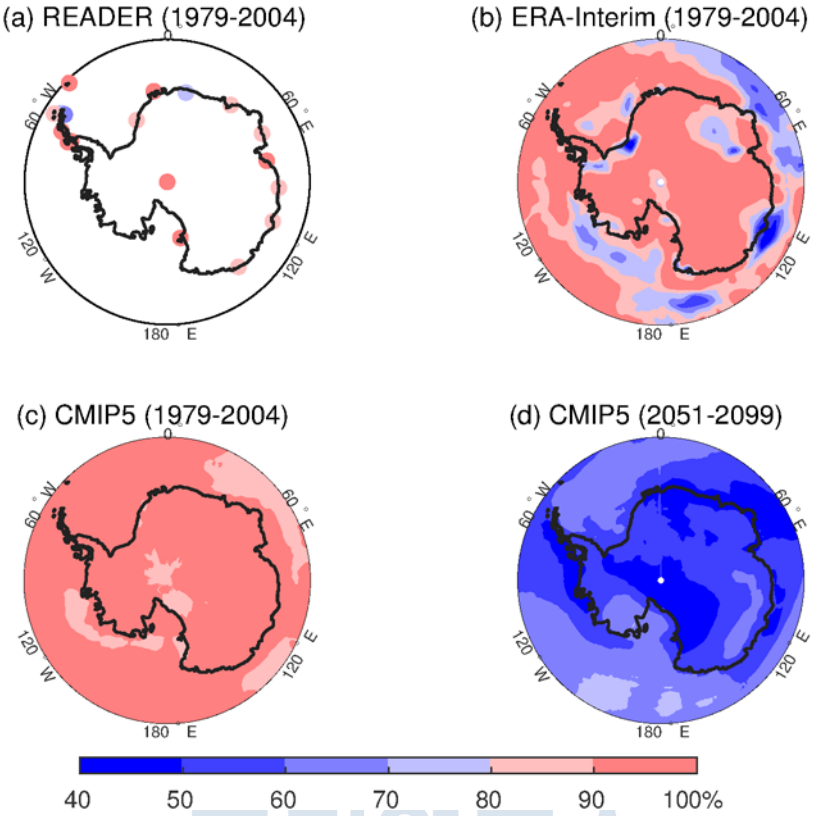

Figure 40. The variance ratio of detrended temperature at the surface (TAS) to original TAS in the austral summer (December to the following February) over the period of 1979-2014 derived by the READER data (a) and the ERA-Interim Reanalysis dataset (b) in the Antarctica. (c) and (d) are ensemble means of variance ratio of detrended TAS to original TAS from 21 CMIP5 models in the austral summer over the periods of 1979-2004 and 2051-2099, respectively.

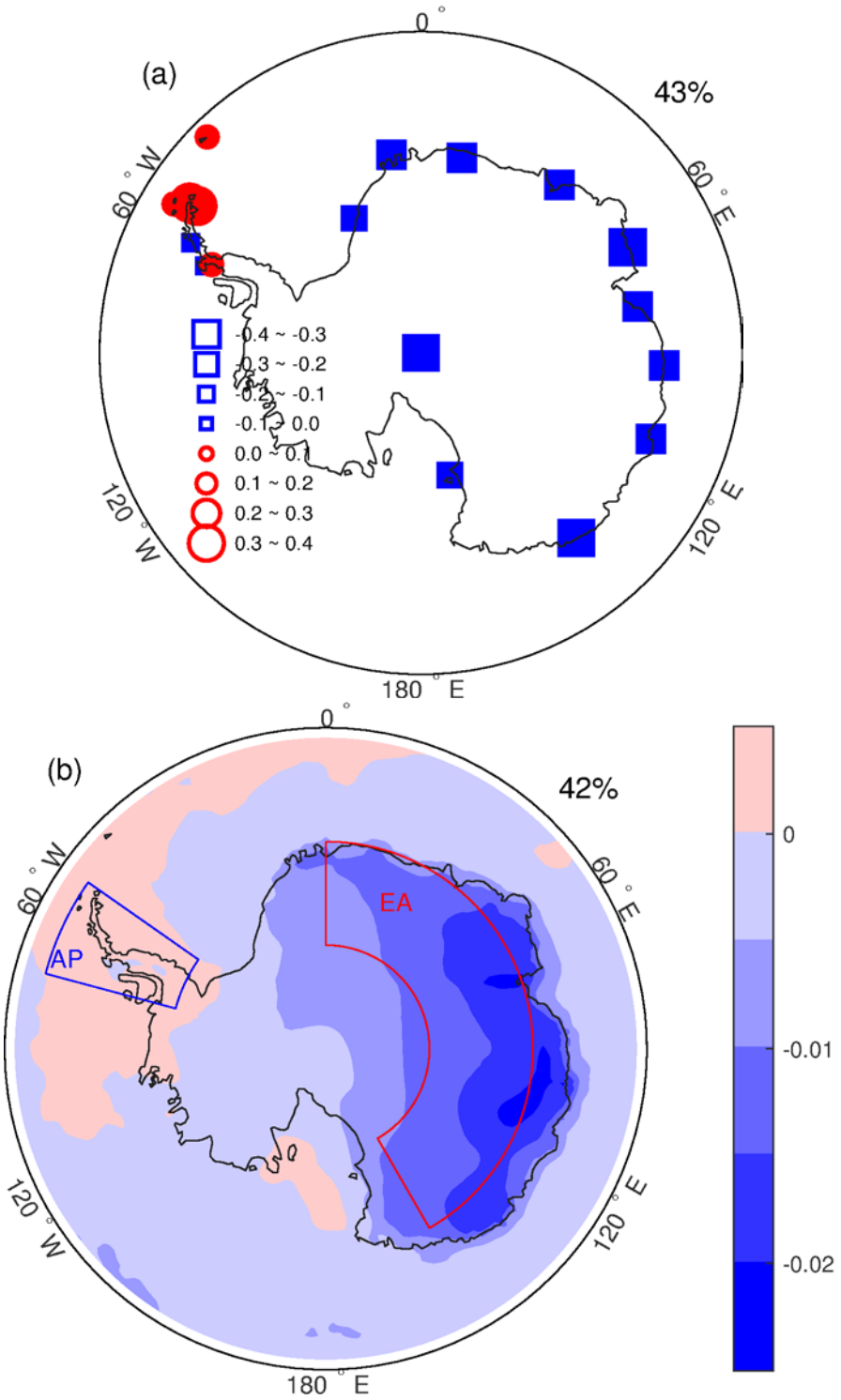
(a)
43%
0 °
60 ° W
60 ° E
120 ° W
120 ° E
180 ° E
-0.4 ~ -0.3
-0.3 ~ -0.2
-0.2 ~ -0.1
-0.1 ~ 0.0
0.0 ~ 0.1
0.1 ~ 0.2
0.2 ~ 0.3
0.3 ~ 0.4
(b)
42%
AP
EA
0
-0.01
-0.02

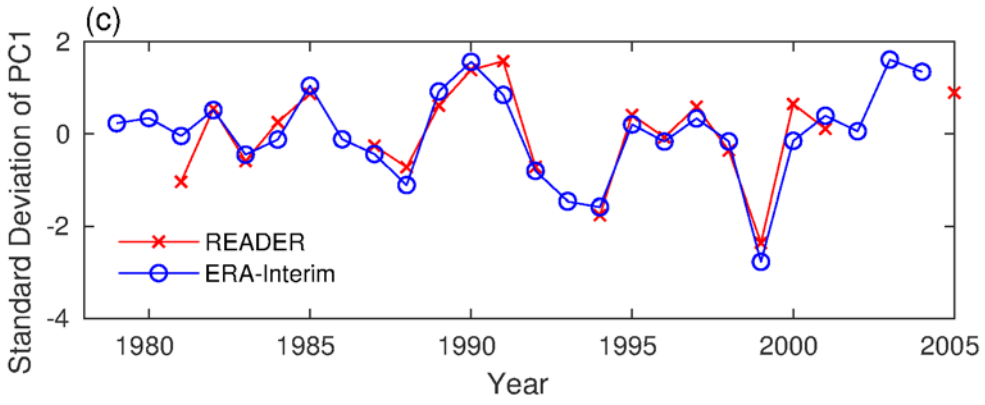

Figure 41. The first mode of variability of detrended temperature at the surface (TAS) in the austral summer (December to the following February) during 1979-2014 derived from the READER data (a) and the ERA-Interim Reanalysis dataset (b) in the Antarctica. (c) shows the time series of the primary components derived from the READER data and the ERA-Interim Reanalysis dataset. Variances are not weighted prior to calculating in (a). R1 (0-150°E and 70°S-80°S) and R2 (80°W-40°W and 62°S-75°S) in (b) indicate the domains of the Eastern Antarctica and the Antarctic Peninsula, respectively.

주 의

1. 이 보고서는 극지연구소 위탁과제 연구결과 보고서입니다.
2. 이 보고서 내용을 발표할 때에는 반드시 극지연구소에서 위탁연구과제로 수행한 연구결과임을 밝혀야 합니다.
3. 국가과학기술 기밀유지에 필요한 내용은 대외적으로 발표 또는 공개하여서는 안 됩니다.